מכון ויצמן למדע

WEIZMANN INSTITUTE OF SCIENCE

Thesis for the degree
Master of Science

חבור לשם קבלת התואר
מוסמד למדעים

By
Raz Alon
Particle Physics Department

מאת
רז אלון
המחלקה לפיסיקה של חלקיקים

חקר הפעולה בגזים אצילים,דימות ורזולוציה זמנית של גלאי קרינה מבוססי מכפיל אלקטרונים מסוג THGEM

Noble-gas operation, timing and imaging properties of Thick Gaseous Electron Multiplier (THGEM)-based radiation detectors

Advisors
Professor Amos Breskin
Dr. Rachel Chechik

מנחים
פרופסור עמוס ברסקין
ד"ר רחל צ'צ'יק

December 2007

כסלו התשס"ח

Submitted to the Scientific Council of the
Weizmann Institute of Science
Rehovot, Israel

מוגש למועצה המדעית של
מכון ויצמן למדע
רחובות, ישראל

Abstract

This work presents the investigations of some properties of the Thick Gaseous Electron Multiplier (THGEM). It is a novel multiplier concept, developed at the Radiation Detector Physics Laboratory at WIS, in which avalanche multiplication occurs within millimeter-scale diameter holes drilled over the surface of a thin, flat insulator.

This work concentrates on the following experimental and simulation studies: time resolution with UV photons and relativistic particles, imaging properties with soft x-rays and preliminary ones with fast neutrons as well as operation in pure noble gases. While the first studies are relevant to numerous general radiation detection applications, the latter relate to their possible incorporation in Dark Matter, double Beta-decay and Neutrino detectors and in noble-liquid Gamma-Cameras.

תקציר

בעבודה זו מוצג מחקר של כמה מתכונותיו של מכפיל האלקטרונים מסוג THGEM. זהו התקן הכפלה-גזית חדיש אשר פותח במעבדת הפיסיקה של גלאי קרינה, בו מתרחשת הכפלת אלקטרונים בתהליך של מפולת (avalanche) בתוך חורים מילימטריים הקדוחים דרך משטח מבודד דק. עבודה זו מתרכזת בעיקר במחקרים הניסיוניים ובסימולציות הבאים: רזולוציה זמנית באמצעות פוטונים בתחום אולטרה סגול וחלקיקים יחסותיים, דימות באמצעות קרני X- רכות, דימות ראשוני של נויטרונים מהירים ופעולה בגזים אצילים. הנושא הראשון שהוזכר הינו רלוונטי למספר יישומי גילוי קרינה כלליים, ואילו הנושא האחרון מתקשר לשילובם האפשרי של המכפלים החדישים בגלאים בתחום חקר החומר האפל, התפרקות ביתא כפולה ופיסיקת הניוטרינו וכן במצלמות גאמא המבוססות על נוזלים אצילים.

Acknowledgements

It is my pleasure to thank all those who assisted me during my M.Sc. thesis research work at the Weizmann Institute of Science. In particular, I would like to extend special thanks:

To my advisors, Prof. Amos Breskin and Dr. Rachel Chechik.

To my lab mates and colleagues, Marco Cortesi, Alexey Lyashenko, Dr. Jun Miyamoto, Dr. Sergei Shchemelinin and Dr. Sana Shilstein.

To Dr. Volker Dangendorf of PTB – Braunschweig, Germany.

To our laboratory technician Moshe Klin.

To the technical staff and electronics lab staff, Yigal Shachar, Eytan Golan, Moshe Sidi, Yafa Gil and Yaron Gal.

And last but not least, to the workshop master Yehuda Asher.

Contents

1. Introduction

Gaseous radiation detectors are widely used in particle physics, astro-particle physics, and other fields, in which very large detection area are required. Examples are high-resolution charged-particle tracking, sampling elements in calorimetry, X-ray and neutron imaging, UV-photon and visible-light imaging detectors etc.

Gaseous Wire Chambers have been in use for almost 40 years. In such chambers, electron avalanche multiplication occurs around widely spaced anode wires inside the chamber. In more modern detectors, generally named "Micro-pattern Gaseous Detectors" (MPGD [1]) multiplication occurs on more densely structured patterned electrodes, e.g. Micro-strip Gaseous Detectors [2], and in some, the multiplication occurs within confined volumes (holes) densely drilled or etched in thin dielectric substrates, as in the GEM (Gas Electron Multiplier) [3] or between very fine mesh electrodes (MICROMEGAS [4]).

The GEM's hole-structure, of low optical transparency, reduces secondary photon-feedback effects (photon-induced generation of secondary electrons in the avalanche process), which are characteristic to wire chambers, and consequently enables higher gains. When two or more GEMs are used in a cascaded mode, the back-flow of ions created in the multiplication process decreases, thus reducing secondary ion-feedback effects. The latter cause damage to the photocathode by direct impact and limits the gain by secondary electron emission, in gaseous photomultipliers; it causes space-charge effects in the detection volume of gaseous detectors (e.g. limiting the resolution of Time Projection Chambers, TPC).

Another advantage of multiplication inside the holes of "hole-multipliers" is the natural pixelation, which enables acquisition of precise position information. This is useful for particle tracking, in time projection chambers, and in many other radiation-imaging systems. The avalanche-multiplication process in "hole-multipliers" is fast, with ns rise times.

The THGEM [5-11] (Figure 1), which is the subject of this research, is a thick version of the GEM. It is made by drilling millimetric (or sub-millimetric) holes in a millimetric (or sub-millimetric) thick Cu-plated G-10 (or other material) printed-circuit board (PCB). The rim around each hole is etched, to avoid possible edge discharges (Figure 1 c). Electrons deposited by radiation in the gas or originating from a solid converter (e.g. a photocathode) are focused into the holes and multiplied

within the holes under the high electric fields (See Figure 2). The field within the hole is created by applying high voltage between the two faces of the THGEM, typically 1000-1500V in 1 atm. Ar/CH_4 (95:5) with 0.4mm thick electrodes.

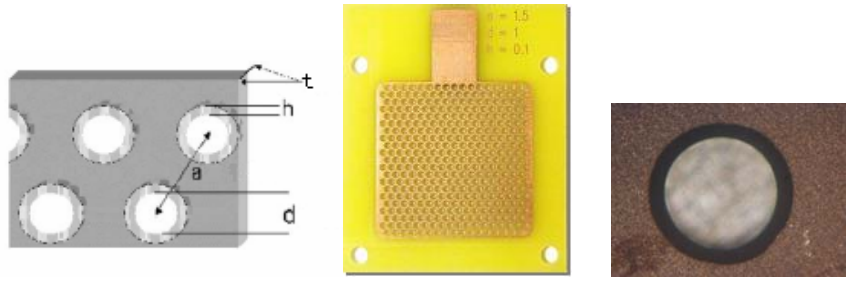

(a) (b) (c)

Figure 1: (a) Schematic view of a THGEM defining the thickness t, hole diameter d, distance between hole centers a and rim width h; (b) THGEM photo with t=1.6mm, d=1mm, a=1.5mm, h=0.1mm; (c) The rim around the hole.

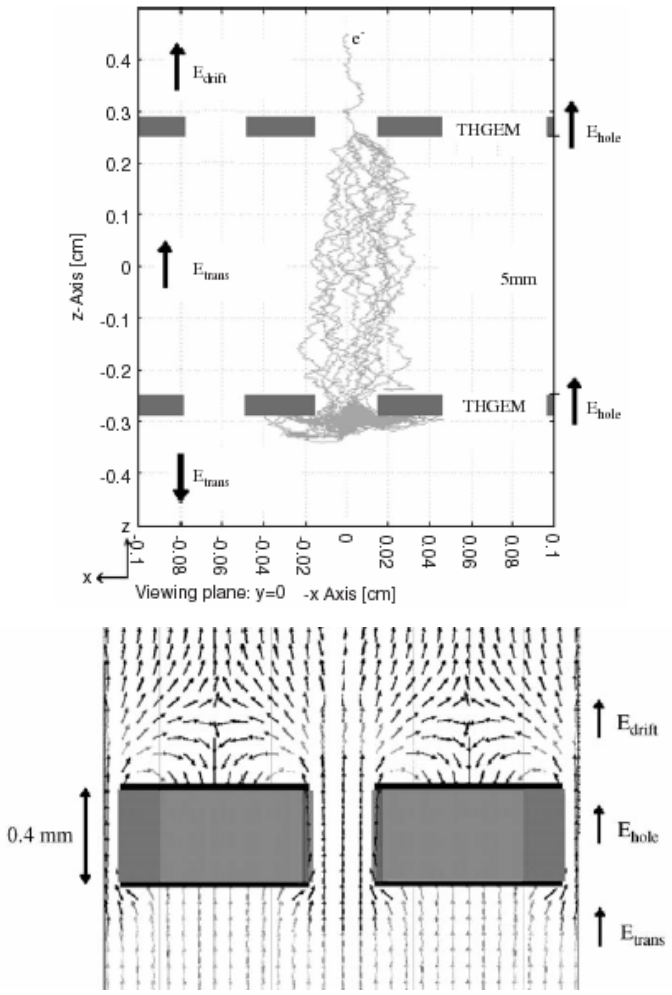

Figure 2: Top: Simulation of electron multiplication with a double THGEM configuration. Bottom: Electric field map inside the THGEM hole and around it [8].

The THGEM has been thoroughly and systematically investigated in the Radiation Detection Physics laboratory at WIS [5-11]. In parallel to the experimental work, simulations were conducted to learn about shape and roles of the different electric fields in the system. The THGEM has been investigated in different gas mixtures and various pressures; the roles of its different geometrical parameters (t, a, d and h, see Figure 1 a) were investigated; Electron transport properties into the holes and that of their transfer into following elements in a THGEM cascade, were studied; gain measurements were taken with different multiplier configurations; ion back flow was studied in some configurations; THGEM's signal rise time and the response to event rate were measured; finally, energy resolution was measured with 6 keV x-rays. Single-electron multiplication factors of up to 10^7 were reached with few-ns rise time. Stable operation was recorded with electron fluxes exceeding MHz/mm^2. Electric fields were optimized for gain and electron transfer efficiency [8-10].

The THGEM is a robust and simple-to-manufacture detector building block. In combination with appropriate radiation converters (coupled to it or deposited on its top surface), it has a variety of potential applications for the detection of UV and visible light, neutrons, X-rays, charged particles, etc. In view of its appeal to many scientific fields and applications, further basic THGEM properties were studied in this Thesis work. Among them: time resolution, imaging properties with soft x-rays and fast neutrons and the operation in noble gases and their mixtures.

2. Methodology

This section describes the general methodology of the operation the THGEM detector. Additional information will be provided in the relevant sections below.

2.1 The THGEM Detector

Measurements were carried out with single- and double-THGEM detector configurations. The double-THGEM detector used here is schematically shown in Figure 3. It is composed of a cathode mesh, two G-10 made THGEMs in cascade, and an anode mesh. In this configuration, the double-THGEM detector can be operated in single-THGEM mode while using the second THGEM top electrode as the anode.

The components are usually mounted inside a stainless steel vessel, unless otherwise mentioned. The detector can be operated under continuous gas flow or in a closed system with internal circulation, as discussed below.

Primary electrons, created by the incident radiation in gas or originating from an appropriate converter, are conveyed by the drift field E_{drift} and focused by the dipole hole field E_{hole} into the THGEM holes, where they are multiplied; typical hole field values are of the order of 20 kV/cm. In a double-THGEM configuration, the avalanche electrons are transferred, after the first multiplication stage, into the second THGEM under the transfer field E_{trans}. Finally, the signal is picked up either on one of the THGEM's electrodes, or on the anode mesh, to which the electrons drift under the induction field E_{ind}.

All meshes and THGEM electrodes (top/cathode and bottom/anode electrode of each THGEM) were biased with independent high-voltage power supplies (CAEN N471A) through 20 MΩ resistors, and the signals were read through decoupling capacitors (Figure 4). Fast reversed diodes were used to protect the preamplifiers against possible discharges.

2.2 ADC Calibration

Most of the analysis in this work was done in pulse-counting mode, i.e. analyzing the signals' pulse height distribution. The signals were recorded through an analog amplification chain, with a multi channel analyzer (MCA). The whole chain was calibrated in order to achieve precise knowledge on the detector's gain.

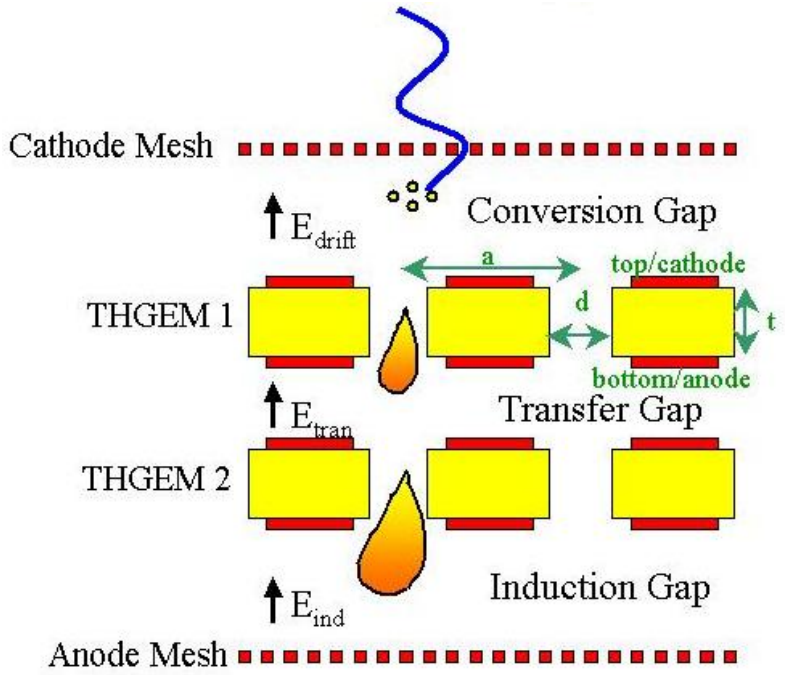

Figure 3: Schematic draw of the double-THGEM Detector; here ionization electrons are deposited in a drift (conversion) gap by absorbed x-rays.

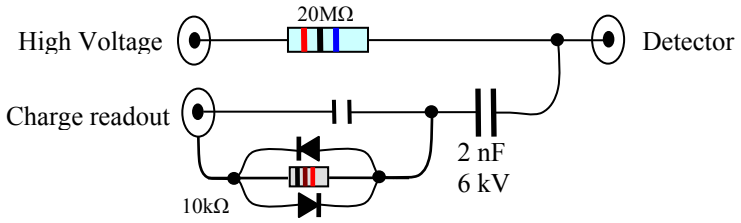

Figure 4: Power and readout circuit.

The calibration scheme is shown in Figure 5. A rectangular pulse from a pulse generator, having an amplitude V, a width of about 1 ms and a rise time of a few ns is injected into an RC circuit, with R=50Ω and C=10pF. The pulse produced by the generator was sometimes affected by a brief surge of current with amplitude higher compared to the value fixed by the user. Since the pulse was then differentiated by the RC circuit, this effect could result in an underestimated injected charge value into the circuit, therefore introducing a small systematic error in the calibration procedure. In order to avoid the described effect an attenuator was inserted between the pulse generator and the RC circuit.

The total charge collected on the capacitor was thus Q = CV. The signals were injected into the readout circuit (Figure 4) and amplified. Ideally, the pulse height generated by the amplifiers is proportional the input charge Q. From the MCA a Gaussian pulse height distribution was obtained. By changing V, and thus Q, a

calibration plot was obtained, from which the ratio of charge per channel, or number of electrons per channel, was deduced.

In order to find the gain of the detector in pulse-counting mode, we assumed the number of primary electrons created by the incoming radiation, e.g. by dividing the energy deposited by incident x-rays by the average energy to produce an electron-ion pair in the gas. The detector's signal was analyzed by the same chain shown on the top of Figure 5, starting with the readout circuit. The pulse-height distribution's peak channel taken from the MCA was multiplied by the electrons per-channel ratio to get the average number of electrons created in the detector's avalanche. Finally, this number was divided by the number of primary electrons to yield the absolute gain.

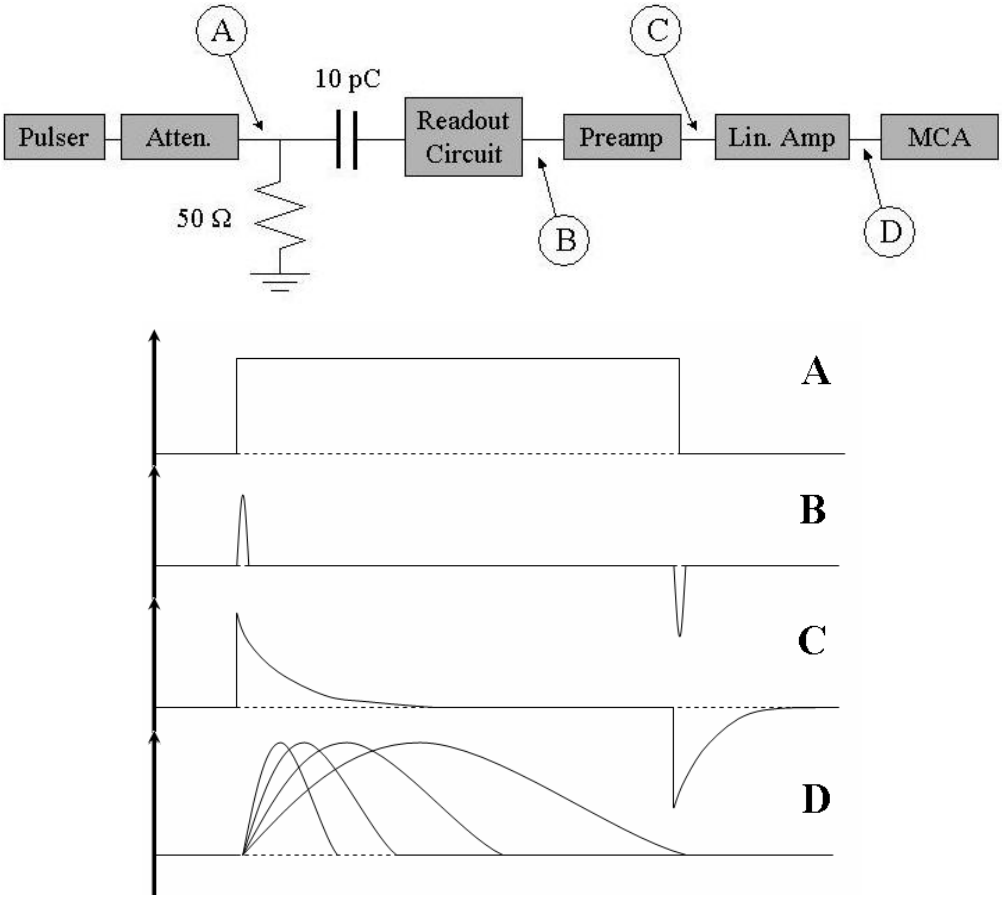

Figure 5: Pulse shapes after different elements in the electronic chain for calibration: (A) Pulse generator output, (B) RC and readout circuits output, (C) Preamplifier output, (D) Linear amplifier output for different shaping time constants

2.3 Signal Shaping in Pulse-counting Mode

The rise-time of the pulse from the preamplifier normally combines the preamplifier's characteristics and the charge collection time in the detector. If the full amplitude of the preamplifier pulse is to be preserved through the shaping process, the shaping time constants of the linear amplifier must be large compared with the preamp's pulse rise-time. Because the shaping time constants cannot always be chosen as arbitrarily large, the amplitude of the shaped pulse can be slightly lower than that attainable with very long time constants. The degree to which the infinite time constant amplitude has been decreased by the shaping time is called ballistic deficit [12].

Signals taken from either of the THGEM electrodes have slower rise-times than those taken from the anode (Figure 6). This is due to the contribution of the slowly drifting ions. It is therefore important to set an appropriate shaping time when taking gain and energy resolution measurements.

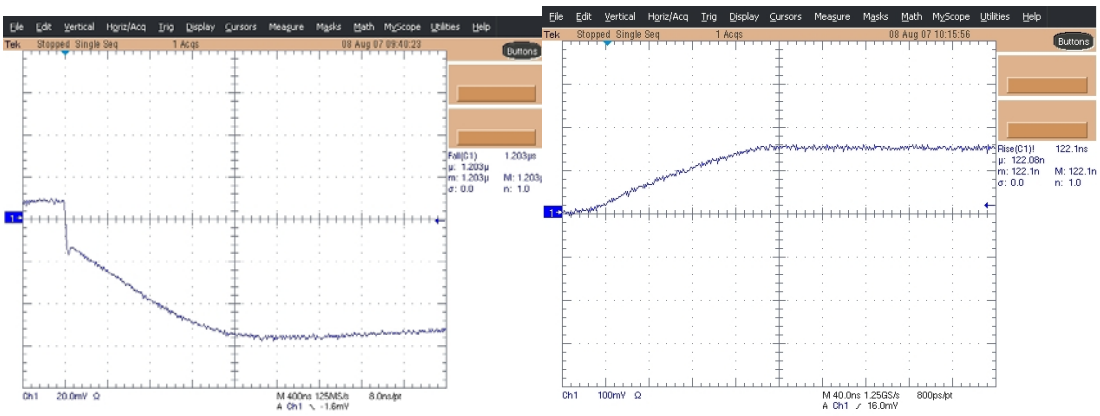

(a) (b)

Figure 6: Preamp signals of the detector. (a) Signal taken from 2nd THGEM top electrode (400ns per division). Note the fast rise due electrons and the slow ion component (b) Signal taken from anode mesh (40ns per division)

Typical absolute-gain curves in Ar/CH_4 (95:5), measured using this calibration mode, are shown in Figure 7. Notice the ~10 fold higher gain measured with the double-THGEM with soft x-rays.

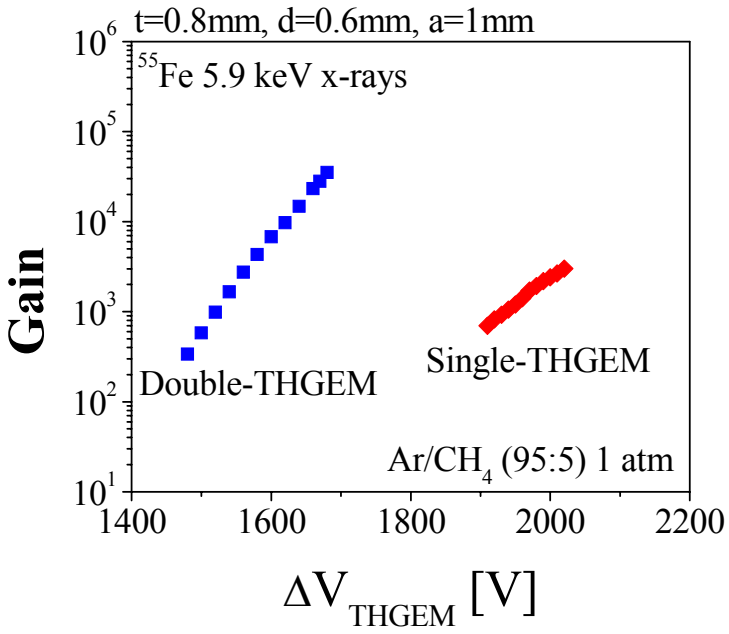

Figure 7: Typical gain curves taken in Ar/CH_4 (95:5) with ^{55}Fe 5.9 keV x-rays at 1 atm., with single- and double-THGEM detectors.

3. Time Resolution

Fast and accurate timing information is required in many applications; a typical example is in high repetition-rate measurements in particle-physics experiments (e.g. at CERN-LHC experiments). In gaseous detectors, the transit time of the primary electrons from their creation point to the readout element is subject to a time jitter, accumulated in the various transport and multiplication steps. The transit-time spread, or time-resolution of a detector, defines the accuracy of timing measurements that can be obtained. While Multiwire Proportional Chambers typically yield resolution times in the several tens of ns range, fast thin-gap resistive-plate chambers (RPC) provide resolution times in the sub-ns scale [13]. Best resolution times reported in cascaded-GEM detectors are of the order of 5ns RMS, measured in particle beams [14, 15]. The latter were measured with GEMs preceded with 3-5 mm wide charge collection gaps (drift gaps); they reflect the statistics of primary and secondary ionization electrons deposition locations along the gap. Time resolution measurements performed with cascaded GEM/CsI photocathode photon detectors in CF_4, with single photons from a pulsed UV lamp, yielded 1.6ns resolution times [16].

The time resolution with THGEM detectors was measured here for the first time for a double-THGEM detector, using a pulsed UV source and minimum ionizing charged particles (MIPs). The latter were either beta-electrons from a ^{106}Ru source or cosmic rays.

3.1 THGEM Time Resolution with UV photons

3.1.1 Methodology

For conversion of UV photons, the detector was equipped with a CsI photocathode, which was either evaporated on a transparent quartz plate and installed 3mm above the first THGEM (semi transparent photocathode), or evaporated directly onto the top surface of the first THGEM (reflective photocathode) [6] (Figure 8). In the case of a semi transparent photocathode, a layer of chromium was evaporated below the CsI in order to bias the photocathode.

Electrons emitted from the photocathode in these two different configurations, travel along different paths and therefore experience different electric fields on their way;

this influences the distribution of the transport time from the photocathode to the THGEM's holes.

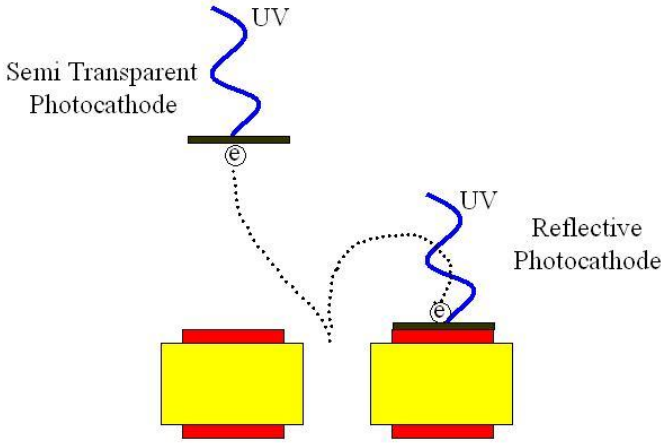

Figure 8: A scheme of a THGEM detector coupled to a semi transparent photocathode (left), or a reflective photocathode (right)

The experimental setup as shown in Figure 9 is composed of the following parts:

1) Fast H_2 flash lamp (emission line peaked at 160nm).
2) Double THGEM detector (t=0.4mm, d=0.3mm, a=0.7mm, Drift Gap = 3mm, Transfer Gap=4mm, Induction Gap = 3.6mm).
3) ESN fast preamplifier (1ns rise time).
4) ORTEC 474 timing filter amplifier.
5) ORTEC 934 quad constant fraction discriminator.
6) ELSCINT time to amplitude converter TAC-N-1
7) Amptek 8000A pocket multi channel analyzer.

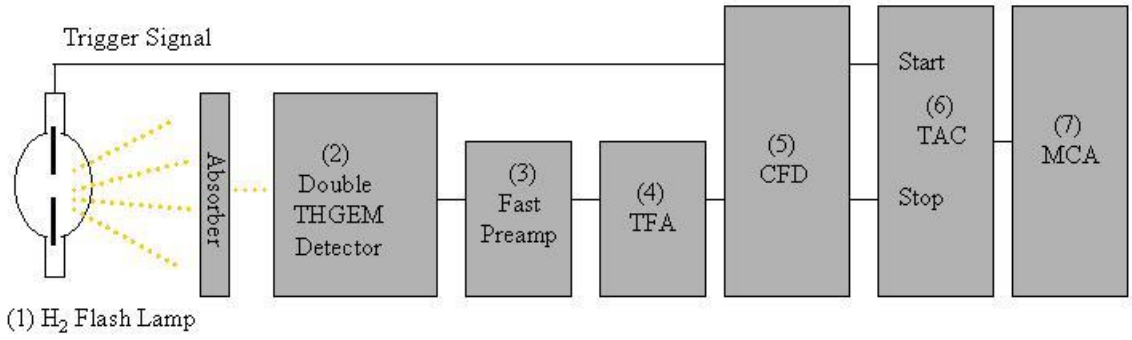

Figure 9: System Setup for Time Resolution Measurements with Photons

By adjusting the light flashes intensity with filters, we could register single- or multiple-photon pulses. This enabled studying the time-resolution dependence on the

number of primary photoelectrons. For this purpose, a calibration step was needed as described hereinafter.

Single-photoelectron avalanche pulse-height spectra follow an exponential distribution; namely the probability for a pulse of height q is proportional to $e^{-q/\bar{q}}$ where $\bar{q}$ is the average pulse height [17]. An example of such a distribution measured with a double-THGEM detector operated in atmospheric Ar/CH_4 (95:5) is given in Figure 10. The data points included in the fit are above the noise and below the tail, to avoid counting of secondary or pile-up pulses.

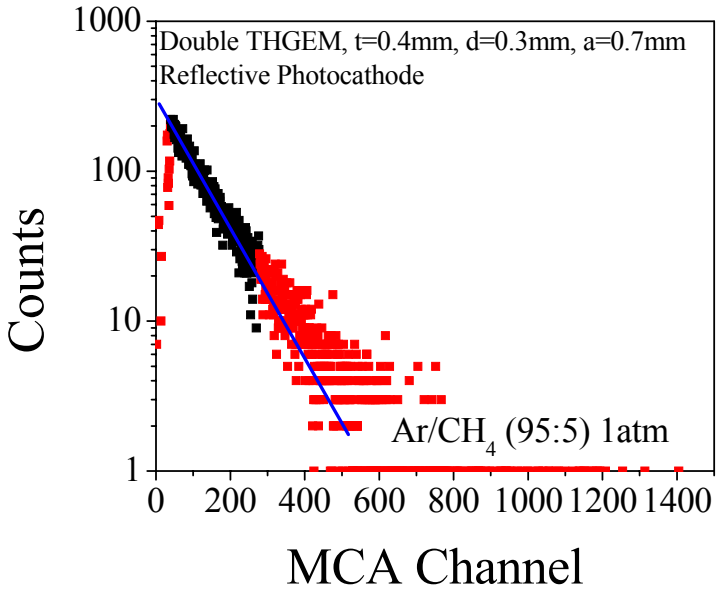

Figure 10: Example of a single-photoelectron avalanche pulse-height spectrum, with an exponential fit (red data points were excluded from fit). Double-THGEM of Figure 9 with a CsI photocathode; atmospheric pressure Ar/CH_4(95:5); detector gain ~10^4.

The spectra were measured for different THGEM voltages and a fit of the average pulse-height $\bar{q}$ (expressed in MCA channels) versus the voltage was used to determine $\bar{q}$ values versus THGEM voltage (Figure 11):

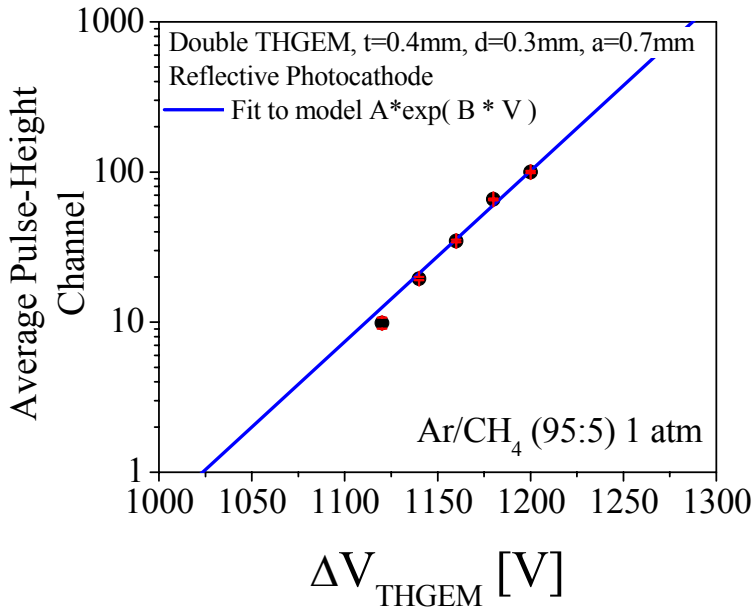

Figure 11: Fit of the average pulse height channel versus voltage

After establishing the working conditions with single primary photoelectrons, the number of avalanche electrons could be increased by increasing the number of photons reaching the detector per light pulse. This was done by removing absorbers and bringing the lamp closer to the detector. The average number of primary photoelectrons for each condition was estimated by dividing the MCA channel of the peak of the pulse-height distribution by the average pulse-height channel $\overline{q}$ obtained in the same detector conditions with single primary electrons.

The pulse-height spectrum was recorded with a Canberra charge-sensitive preamplifier followed by an ORTEC 571 linear amplifier, which was further connected to the Amptek 8000A pocket MCA.

Following this calibration stage, the detector time resolution as function of the number of photoelectrons per pulse was determined with the setup shown in Figure 9 above. The time resolution, σ, is the standard deviation of the distribution of the time difference between the detector signal and the trigger signal.

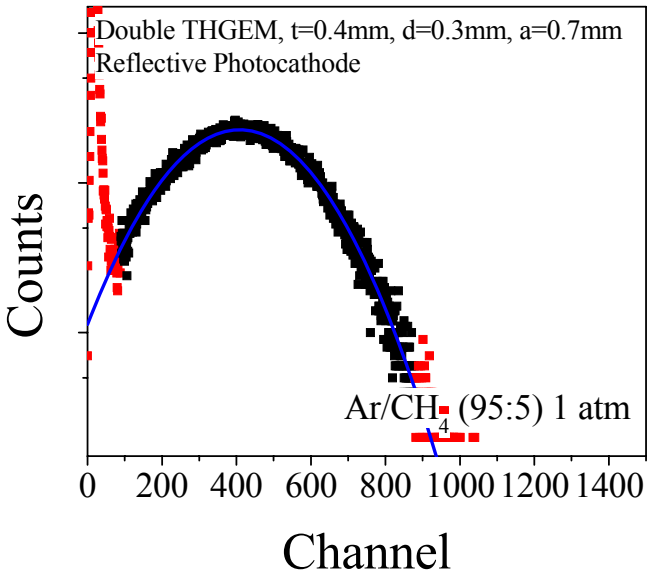

Figure 12: Example of a pulse-height spectrum recorded with multiple primary photoelectrons with a Gaussian fit (red data points were excluded from the fit)

3.1.2 Results

This section presents experimental measurements and simulated data of time resolution, using semitransparent and reflective photocathodes. The effects of the number of primary photoelectrons, and that of the different electric fields in the detector, on the time resolution are shown. Simulated data are compared to the experimental results.

3.1.2.1 Reflective Photocathode

The data in Figure 13 were taken with a bias of 1190V on both THGEMs with a CsI photocathode deposited on the top surface (Figure 8 right). The drift field was set to zero, as recommended for best electron transport into the holes [8]. The transfer field was 3000 V/cm and a reversed induction field of –200 V/cm was applied. Signals were recorded from the bottom electrode of the 2nd THGEM. Due to high noise in the single photoelectrons measurement, there was a big uncertainty on the fitted data.

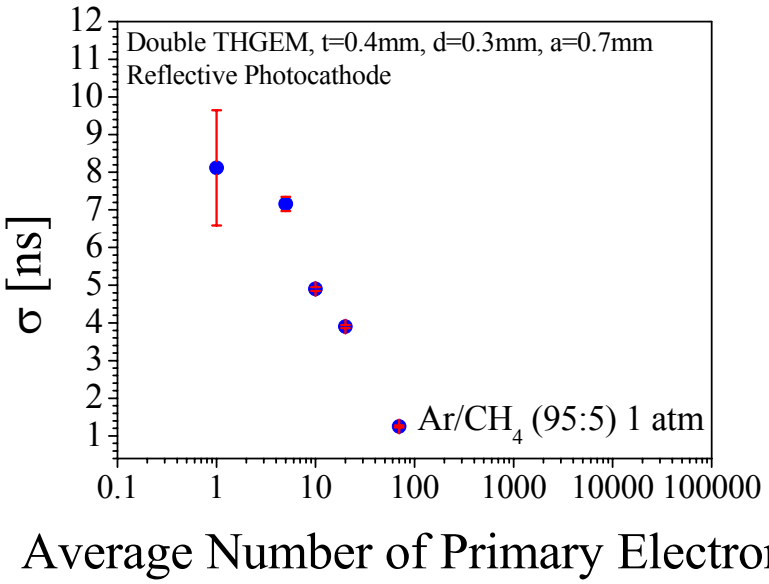

Figure 13: Time resolution versus average number of primary electrons, in a double-THGEM with a reflective photocathode deposited on its top surface (shown in Figure 8 right)

Calculating the field on the THGEM surface (Figure 14) and the drift velocity of electrons at such high fields (Figure 15) it was suggested that those electrons which are emitted from a reflective photocathode closer to the holes, may have a shorter drift time both from the shorter path they take into the holes, and from their higher drift velocity.

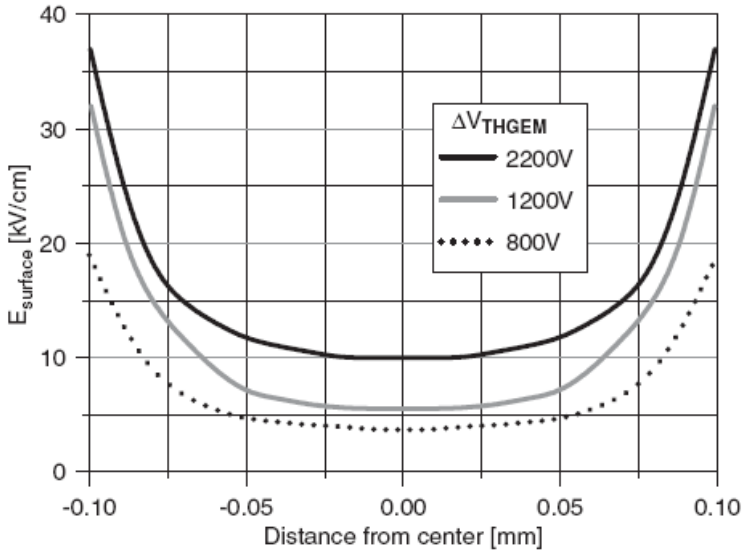

Figure 14: Simulated electric field on THGEM surface versus distance from hole center [8].

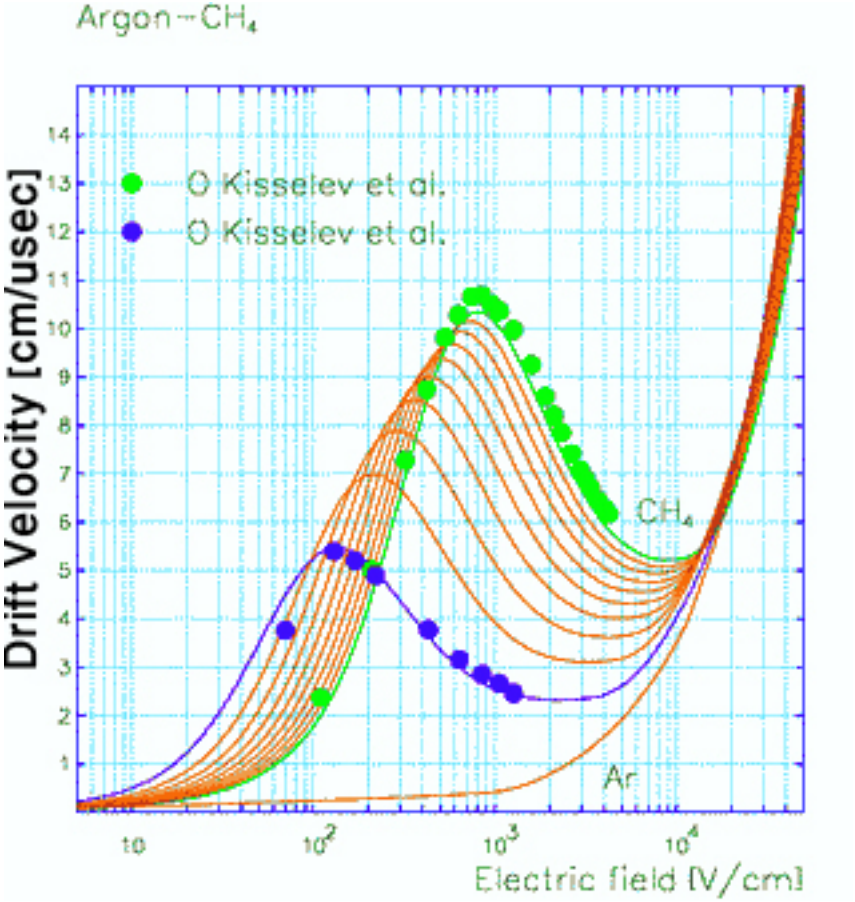

Figure 15: Calculated drift velocity of electrons in Ar/CH_4 versus electric field, at 20°C 760 Torr, varying from pure Ar to pure CH_4 in steps of 10% [20].

GARFIELD [19] simulation was used to study this point. In the following simulations, the THGEM geometry used was t=0.4mm, d=0.3mm, a=0.7mm. Assuming the photocathode is exposed to the incoming photons uniformly, more photoelectrons will originate from the larger distances from the hole center (photosensitive area increasing quadratically in proportion to the distance). Electrons were set accordingly on the THGEM surface, along the line connecting two holes' centers. The bias on the THGEM was set to 1230 V and the drift field was set to zero. Figure 16 shows the simulated drift-time distribution of electrons emitted from the THGEM surface into the holes.

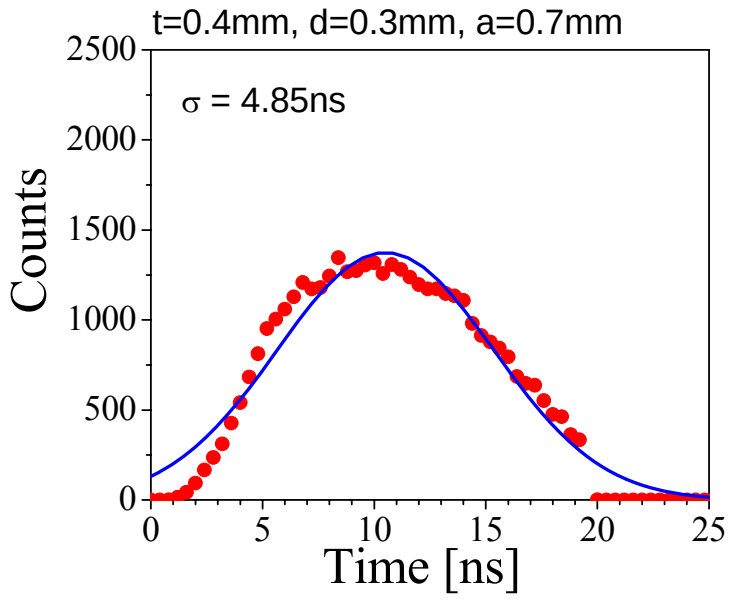

Figure 16: Simulation results of electrons' drift time distribution from the THGEM surface into the holes. The simulated gas is Ar/CH_4 (95:5) at 1 atm. with ΔV_{THGEM}=1230V and E_{drift}=0. THGEM geometry is shown in the figure.

Figure 17 shows the drift-time distributions of electrons emitted closer to the holes (up to one quarter of the total holes' pitch), and those emitted farther from the holes (over one quarter of the total holes' pitch).

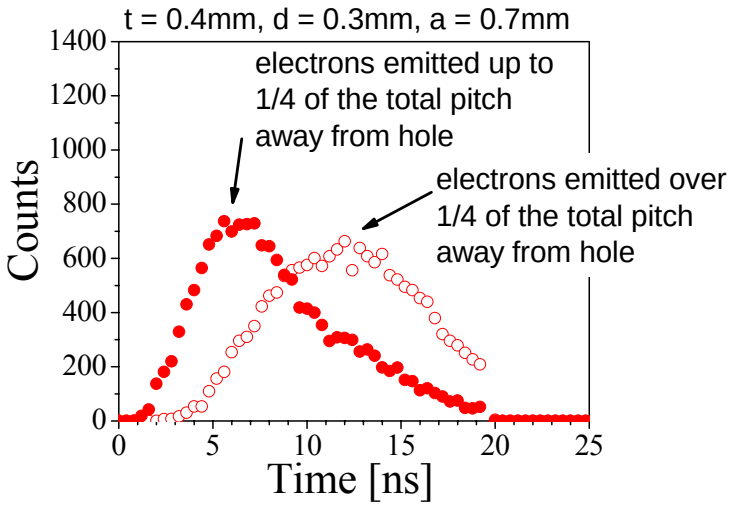

Figure 17: Electrons' drift time from THGEM surface into holes, for electrons emitted closer to and farther from holes. The simulated gas is Ar/CH_4 (95:5) at 1 atm. with ΔV_{THGEM}=1230V and E_{drift}=0. THGEM geometry is shown in the figure.

3.1.2.2 Semitransparent Photocathode

The data in Figure 18 were taken with a double-THGEM coupled to a semitransparent photocathode placed at 3mm above the first THGEM (shown in Figure 8 left). A bias of 1250V was applied on both THGEMs. The drift field was 1000 V/cm, the transfer field was 3000 V/cm and a reversed induction field of –200 V/cm was applied. Similarly, in Figure 19, a lower drift field, of 200 V/cm, was applied, to study the effects of the drift velocity on time resolution.

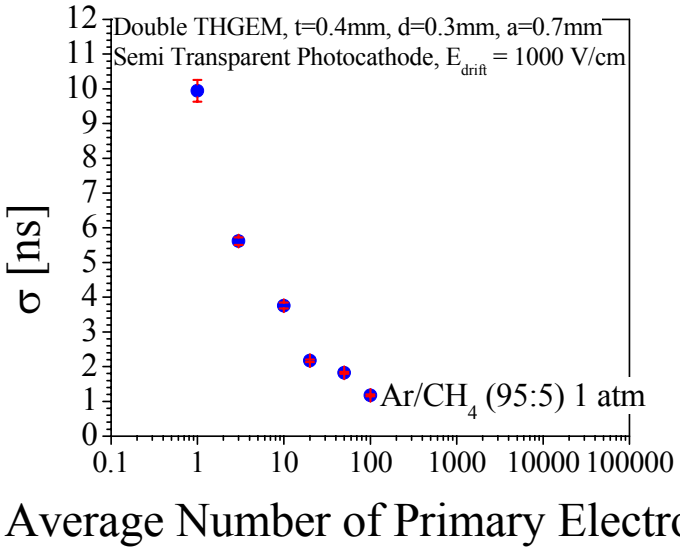

Figure 18: Time resolution versus average number of primary electrons, in a double-THGEM coupled to a semi transparent photocathode, E_{drift}=1000 V/cm

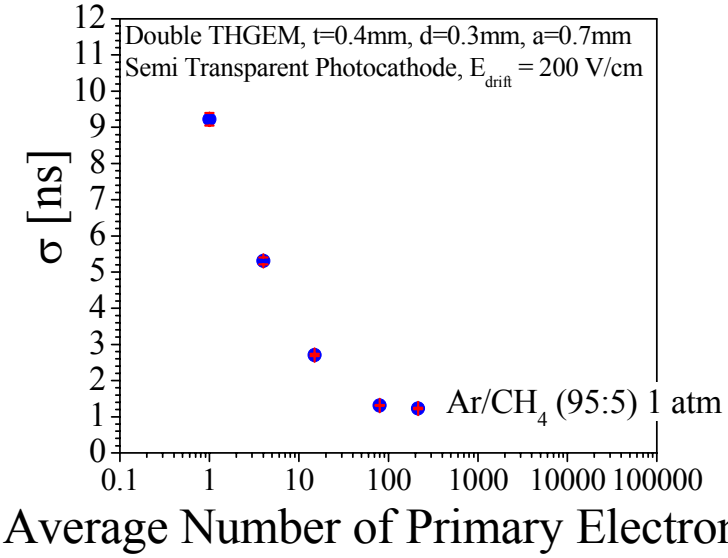

Figure 19: Time resolution versus average number of primary electrons, in a double-THGEM coupled to a semi transparent photocathode, E_{drift}=200 V/cm

The experimental data in Figure 20 shows single photoelectron time resolution, versus the drift field, with a bias of 1300V on both THGEMs. The transfer field was 3000 V/cm and a reversed induction field of –200 V/cm was applied. Also shown in Figure 20 are simulation results; the electric fields for this detector's configuration were calculated using Maxwell [18], and electrons drift path was simulated by GARFIELD [19]. In the drift path simulations, electrons were deposited uniformly 3mm above the THGEM surface, and their drift lines into the THGEM's holes were simulated, while recording the drift times (examples of electron paths generated by GARFIELD are shown in Figure 2). The RMS values of these time distributions are shown in Figure 20. Similarly, in Figure 21, the drift field was kept at 500 V/cm and the time resolution was measured as function of the transfer field.

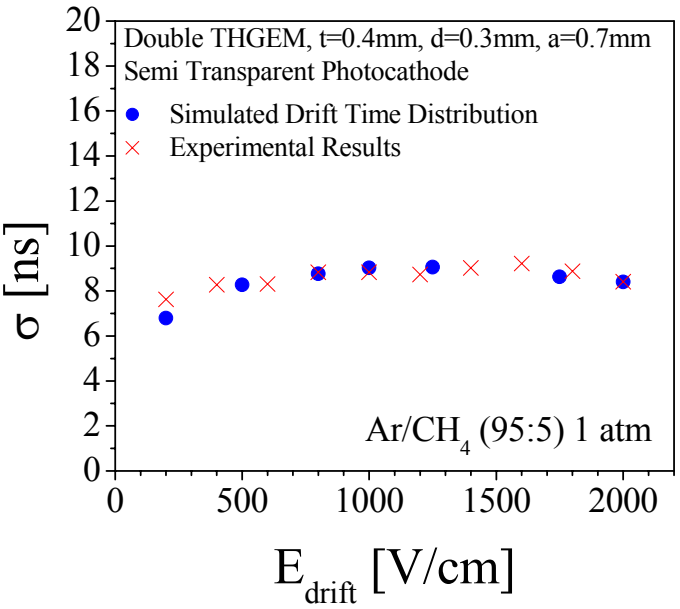

Figure 20: Measured single electron time resolution versus E_{drift}, in a double-THGEM coupled to a semi transparent photocathode. Simulation results are shown as well

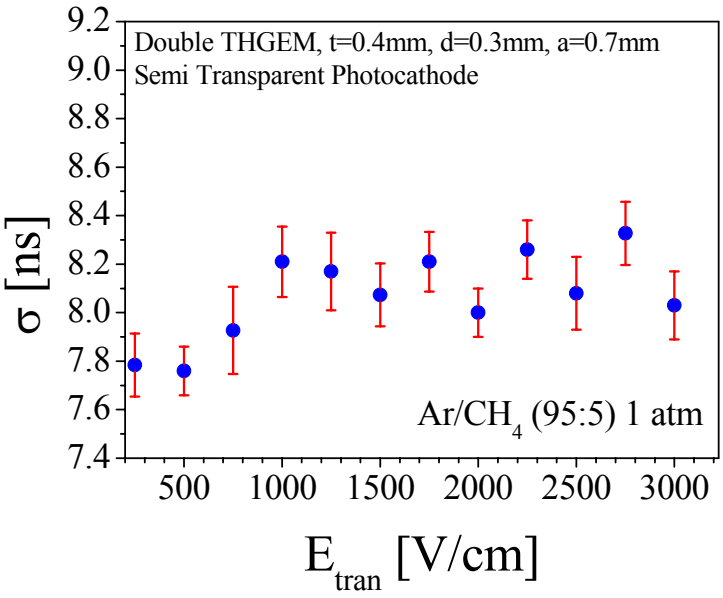

Figure 21: Measured single electron time resolution versus E_{tran}, in a double-THGEM coupled to a semi transparent photocathode

3.1.3 Discussion of the time resolution with photocathodes

As shown in Figure 13, Figure 18 and Figure 19, the time resolution measured with a double-THGEM with single photoelectrons varies between 8ns to 10ns (RMS). With about 100 photoelectrons, it goes down to about 1ns (RMS). This is due to triggering always on the fastest photoelectrons (the first ones reaching the THGEM hole). At lower gains it was possible to increase the number of primary photoelectrons per pulse to values above 1000; e.g. in that case (not shown here), the time resolution with 2000 photoelectrons was 0.54ns (RMS).

As expected, there is a difference of ~7ns in the average drift time of the two groups of electrons in Figure 17, those emitted closer to the hole, and those emitted farther from the hole. Their respective RMS widths are 3.47ns and 4.15ns.

Comparing between Figure 18 and Figure 19, there is an improvement of the time resolution of single photoelectrons, at lower drift fields. This may be due to the faster drift velocity of electrons in these conditions, as shown in Figure 22 (5 cm/μsec at 200 V/cm compared to ~2.5 cm/μsec at 1000 V/cm, with Ar/10% CH_4). The effect of the faster drift velocity can also be seen in Figure 20 and Figure 21. As the drift velocity decreases at fields between 200 V/cm to 1000 V/cm, the time resolution worsens. In Figure 20 it slightly changes from about 7.6ns to 8.8ns and in Figure 21

from about 7.8ns to 8.2ns. Above 1000 V/cm the average RMS value reaches saturation, which is also in agreement with the drift velocity and the simulated data.

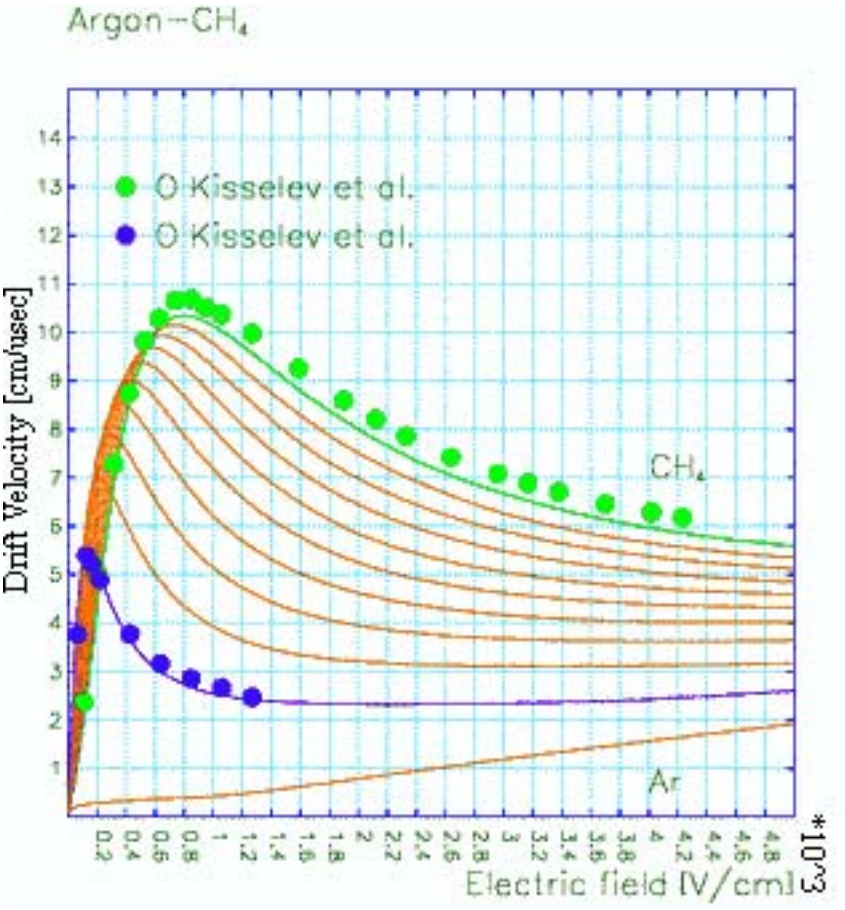

Figure 22: Calculated drift velocity of electrons in Ar/CH_4 versus electric field, at 20°C 760 Torr, varying from pure Ar to pure CH_4 in steps of 10% [20]

These results include the time width (photon time distribution) of the light pulses of the lamp. The width of the lamp pulse, composed of many "single photons" was measured with a PMT; it had an estimated RMS value of about 2ns (Figure 23).

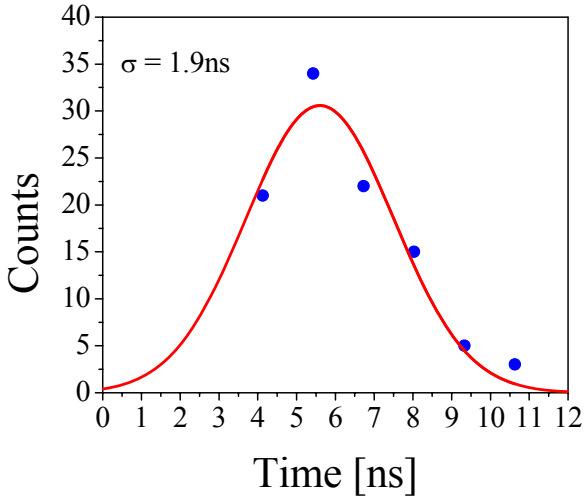

Figure 23: H_2 lamp pulse width.

While detecting single or a few photons emitted from the lamp, the expected time jitter due to the lamps is large as these few photons are distributed over the lamp's emission impulse width (e.g. ~2ns RMS). For large numbers of photons, the first emitted photons are those that contribute to the detector's pulse buildup (pulse rise), such that the lamp's pulse width has practically no influence on the measured time resolution.

Therefore, the time-resolution values presented in Figure 13 and Figure 19, for small numbers of photons, should be corrected, while those for large photon numbers are naturally only little affected by the pulse width of the lamp; as reflected in Equation 1, a quadratic correction for the 2ns (RMS) lamp jitter on a measured 10ns (RMS) resolution is negligible.

$$\sigma_{corrected} = \sqrt{\sigma^2_{measured} - \sigma^2_{lamp}} = 9.8ns$$

Equation 1

3.2 THGEM Time Resolution with MIPs

The THGEM detector is considered, among others, for relativistic charged-particle (e.g. muon detection at LHC) tracking at high repetition rates. This requires studies of its time response.

Electromagnetic interaction is generally used as the basis for detection of charged particles, being many orders of magnitude more probable than strong or weak interactions. In tracking detectors particles lose part of their energy in the conversion

(drift) region. An expression for the average differential energy loss (loss per unit length) due to Coulomb interactions with gas molecules was proposed by Bethe and Bloch [21] in the framework of relativistic quantum mechanics, and can be written as follows (in electrostatic unit system):

$$\frac{dE}{dx} = -K\frac{Z}{A}\frac{\rho}{\beta^2}\left(\ln\frac{2mc^2\beta^2 E_M}{I^2\left(1-\beta^2\right)} - 2\beta^2\right);\ K = \frac{2\pi N z^2 e^4}{mc^2}$$

Equation 2

Where N is the Avogadro number, m and e are the electron mass and charge, Z, A and ρ are the atomic number and mass, and the density of the medium, respectively, and I is its effective ionization potential; z is the charge and β the velocity (in units of speed of light c) of the projectile. In the electrostatic unit system and expressing energies in MeV, $K = 0.154$ MeV gr^{-1} cm^2 for unit-charge projectiles. In the system used, the rest energy of the electron, mc^2, equals 0.511 MeV.

The quantity E_M represents the maximum energy transfer allowed in each interaction, and simple two-body relativistic kinematics gives

$$E_M = \frac{2mc^2\beta^2}{1-\beta^2}$$

Equation 3

Inspection of Equation 2 shows that the differential energy loss depends only on the projectile velocity β, and not on its mass. After a fast decrease dominated by the β^{-2} term, the energy loss reaches a constant value around $\beta \approx 0.97$ (Figure 24) and eventually slowly increases for $\beta \rightarrow 1$ (relativistic rise). The region of constant loss is called the minimum ionizing region and corresponds to the more frequent case for relativistic minimum ionizing particles (MIPs) in high-energy physics.

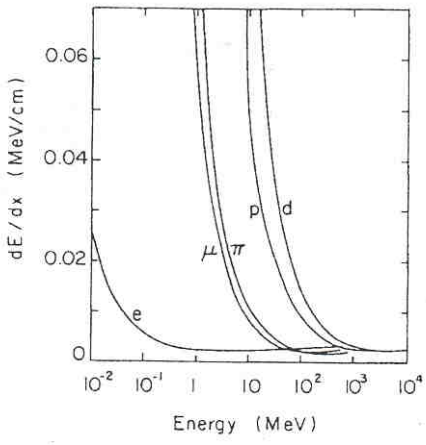

Figure 24: Energy loss per unit length in air, as computed from Equation 2, for different particles as a function of their energy. At energies above 1 GeV/c or so, all particles lose about the same amount of energy (minimum ionization plateau) [21].

As a practical example, 1 MeV electrons leave about 675 eV while traveling through 3mm of Ar at 1 atm [22]. Assuming all this energy is used for ionization, this yields 26 primary electrons in the gas.

We carried our experiments at the lab with cosmic rays and with Beta-particles from a ^{106}Ru source. Beta sources are the most common emitters of fast electrons in radiation measurements, consisting of radioisotopes, decaying by beta-minus emission. The process is written schematically:

$$ {}^{A}_{Z}X \rightarrow {}^{A}_{Z+1}Y + \beta^{-} + \overline{\nu} $$

Equation 4

where X and Y are the initial and final nuclear species, and $\overline{\nu}$ is the antineutrino [12]. It has an extremely small interaction probability with matter and is practically undetected for our purposes. Y has a very small recoil energy, which is ordinarily below the ionization threshold, and cannot be detected by conventional means. The only significant ionizing radiation produced by beta decay is the beta particle itself.

The decay energy is shared mainly between the beta particle and the antineutrino. The beta particle energy has a distribution, of which the high energy tail is called endpoint energy, and is numerically equivalent to the decay energy. The mean energy is usually much lower. See Figure 25.

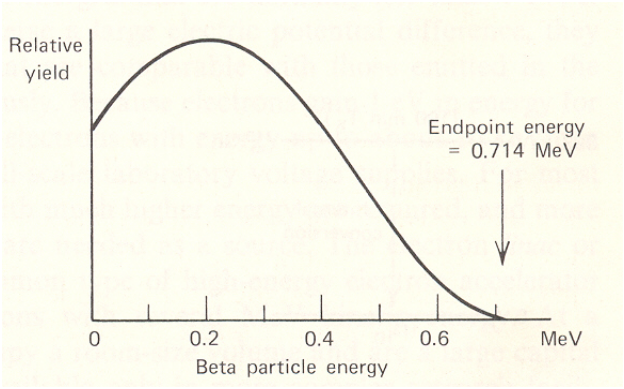

Figure 25: Example of a Beta-particle spectrum of ^{36}Cl

The ^{106}Ru source used has a half-life time of ~1 year. ^{106}Ru decays into ^{106}Rh which has a half life time of 30 seconds [23]. The resulting Beta electrons are distributed as follows:

Energy (MeV)	Percentage
2.00	3%
2.44	12%
3.10	11%
3.53	68%
Other	6%

Table 1: Energy distribution of Beta electrons from a ^{106}Ru decay [23]

Cosmic rays are charged particles such as protons and heavier nuclei (up to gallium), as well as photons and neutrinos present throughout the galaxy, which enter into earth's atmosphere, creating showers of charged particles such as electrons and muons. Cosmic rays have a broad energy spectrum and can get over 10^{20} eV.

3.2.1 Methodology

The compact MIPs detector we built for time resolution measurements is a double-THGEM with t=0.4mm, d=0.3mm, a=0.8mm. The conversion, transfer and induction gaps were 3mm each. In order to have a compact measuring geometry, and to position the PMTs as close as possible to the detector, the detector's parts were assembled with epoxy glue (Figure 26), and mounted on a dedicated stand. Small tubes allowed for efficient gas flow.

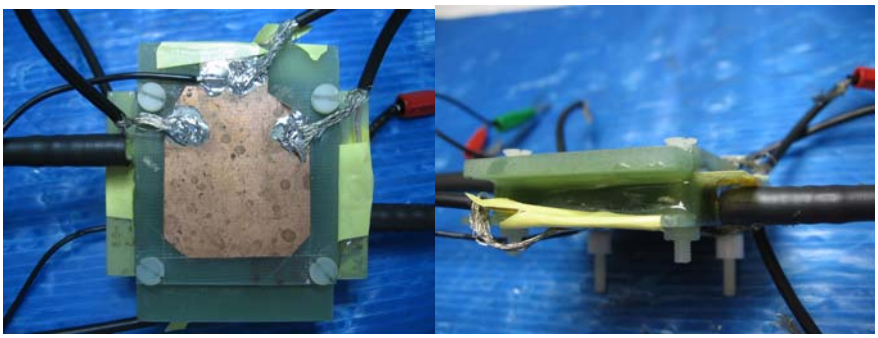

Figure 26: Top and side views of the MIPs detector

For comparison, a similar detector was assembled with 3 standard GEMs (70 micron holes' diameter, 140 micron apart). It had a 3mm conversion gap; two transfer gaps of 1.6mm each and an induction gap of 4.6mm.

In all measurements, atmospheric Ar/CH_4 (95:5) was used.

Two methods of analysis were used. The "online" analysis system setup is shown in Figure 27, with signals amplified with a low-noise VV43 fast preamplifier (MPI – Heidelberg), shaped, discriminated and analyzed with a time-to-amplitude converter (TAC) followed by a multichannel analyzer (MCA). The third element in the chain in Figure 27, the PMT, was coupled to a 4.7mm thick plastic scintillator.

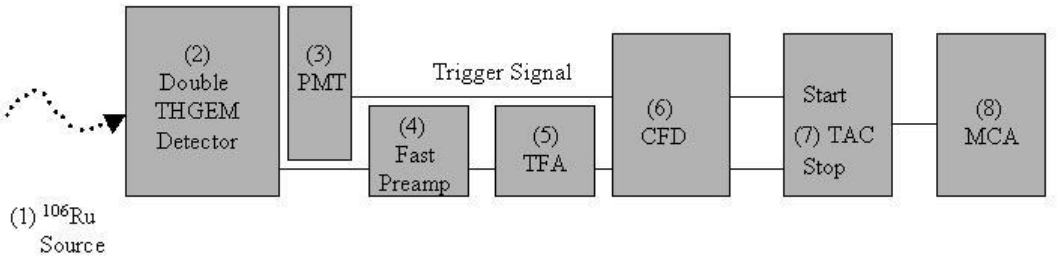

Figure 27: System setup for time resolution measurements with ^{106}Ru using online analysis. The PMT was coupled to a 4.7mm thick plastic scintillator.

Results with the above setup are shown below. Observation of the analog signals (Figure 28) revealed a strong pulse-to-pulse variation of signal rise-time, shape and amplitude. These are due to the statistical fluctuations in the deposition location of primary and secondary electrons and that of the avalanche buildup. It therefore made it very difficult to adjust the parameters of the constant fraction discriminator, which as a matter of its operation principle, only performs well with pulses of uniform pulse shape.

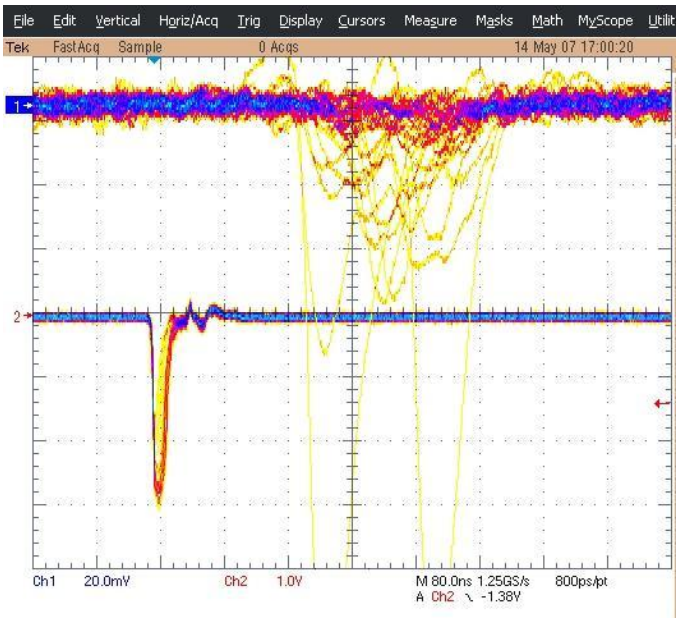

Figure 28: Different shapes and rise-times of gas detector signals seen in Channel 1 (top). The trigger PMT analog signal is shown in Channel 2 (bottom).

An attempt to filter out particles with energy of less than 1 MeV, using an absorber (e.g. a 2-2.5mm G-10) in front of the triggering PMT, did not yield any significant improvements in the measured time spread.

Consequently, a second analysis method was employed, the "offline" method, in which the wave forms of the signals were recorded on a digital scope, and processed offline using Matlab programs. The setup shown in Figure 29 had the following additional components:

1. Hamamatsu R980 PMT coupled to a 4.7mm thick plastic scintillator.
3. Hamamatsu R6095 PMT coupled to a 4.7mm thick plastic scintillator.
7. LeCROY 622 quad coincidence unit.
8. Tektronix TDS5054B digital oscilloscope.

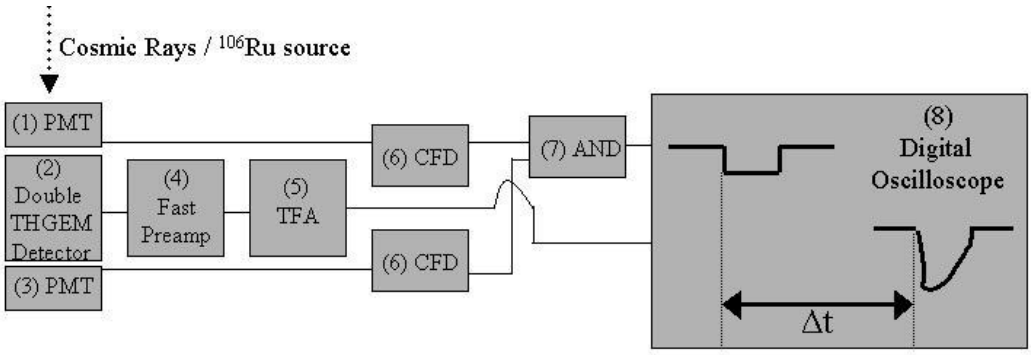

Figure 29: System setup for time resolution measurements with cosmic rays and ^{106}Ru using offline analysis. The same system was used for the THGEM and the GEM detectors.

Using the two PMTs/scintillators in coincidence helped filtering out spurious events.
The algorithm used in the offline analysis for finding the onset of the signal was as follows. First, a threshold was set, e.g. one standard deviation below the average "zero" voltage level. Then, the peak was found (the absolute minimum point of the negative signal). Finally, the onset of the signal was set to be the first point before the peak, which was above the threshold.
In order to avoid further possible deterioration of the time resolution due to electron drift in the induction gap, the signals were taken from the second THGEM's top electrode in the double-THGEM detector, and the third GEM's top electrode in the triple GEM detector. The multipliers were biased asymmetrically (different potentials across each element) in order to reduce the effect of conversions in the transfer gap, yielding low-amplitude detector signals due to multiplication in fewer multiplication steps.
In the first set of measurements, changes were made to one of the following three parameters – E_{drift}, E_{tran}, and the CFD threshold, while the other two parameters were kept constant. Variation of the two electric fields allowed for studying their influence on the time resolution. As seen in Figure 22, for Ar/10% CH_4 the drift velocity at 200 V/cm peaks at about 5 cm/μsec, and drops to 2.5 cm/μsec and below for fields above 1000 V/cm. In general, shorter drift times result in smaller time fluctuations. Variation of the CFD threshold allows studying the effect of low-amplitude detector signals.

3.2.2 Results with the ^{106}Ru Source

In the following results measured in atmospheric Ar/CH_4 (95:5), the voltages on the THGEMs were ΔV_{THGEM1}=1260V, ΔV_{THGEM2}=1060V. A reversed induction field of -200 V/cm was applied.

3.2.2.1 Varying CFD threshold, Fixed E_{drift} and E_{tran}, online analysis

Figure 30 shows the time distributions at a fixed drift field of 500 V/cm and transfer field of 2000 V/cm, while the detector CFD threshold was increased. The distributions were asymmetric and had a small tail on the right (to be discussed). They were fitted with a Gaussian (excluding the tail), and its RMS value, σ, is shown in the figure.

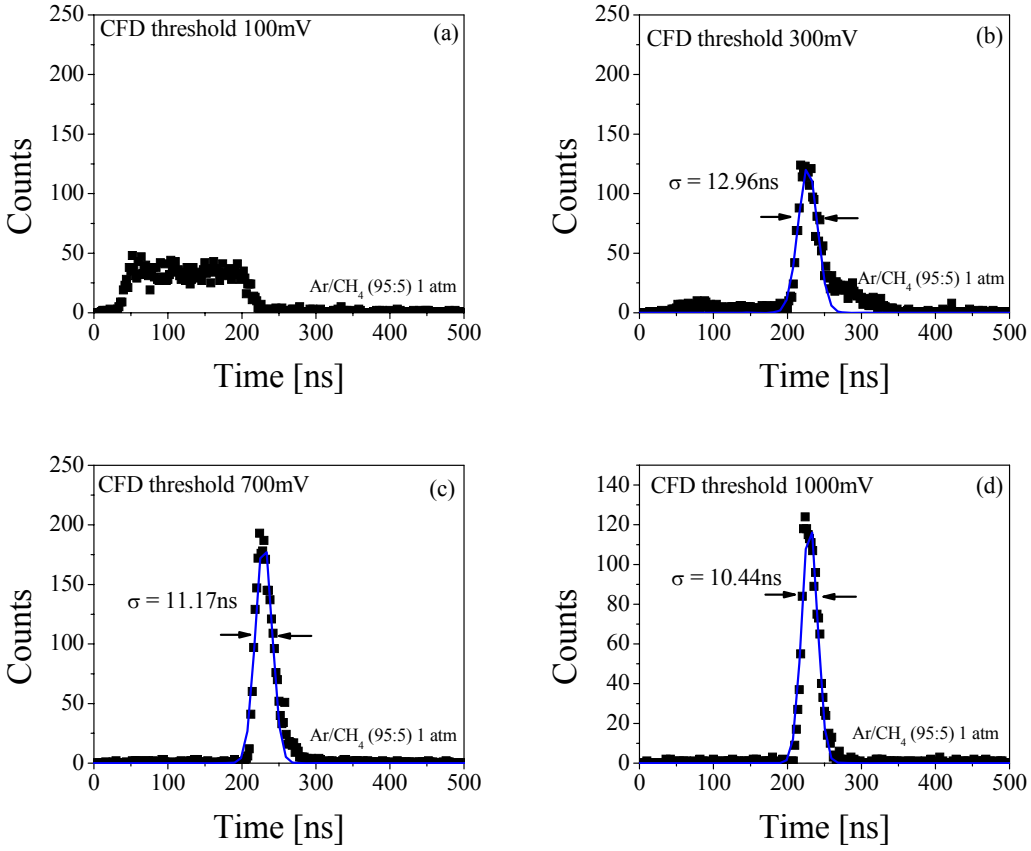

Figure 30: Time resolution at fixed drift and transfer fields, varying CFD threshold: (a) 100mV, (b) 300mV, (c) 700mV, (d) 1000mV

All plots but (d) have the same vertical scale and depict approximately the same total number of counts. The distributions' fitted RMS values improve as the threshold is increased. The events on the left side of the spectra, visible at low thresholds, disappear as is the threshold increases; they are related to noise. The tails on the right side become smaller as the threshold increases, implying that their origin could be of low-amplitude detector signals. As shown in the practical example in section 3.2, the MIPs deposit only a small amount of energy in the detector, resulting in a small number of primary electrons (about 26 primary electrons for 1 MeV incident electrons over a gap of 3mm). Examining Figure 10 we see that for the typical exponential single-electron pulse-height distribution, the vast majority of the pulses have very low amplitudes. In many cases these low signals cannot be discriminated from the noise. Furthermore, occasional high pulses, originating from delta electrons, created at different locations along the drift gap, worsen the time resolution.

3.2.2.2 *Varying E_{tran}, Fixed E_{drift} and CFD Threshold, online analysis*

Figure 31 shows the time distributions at a fixed drift field of 500 V/cm and CFD threshold of 500 mV, for different transfer fields:

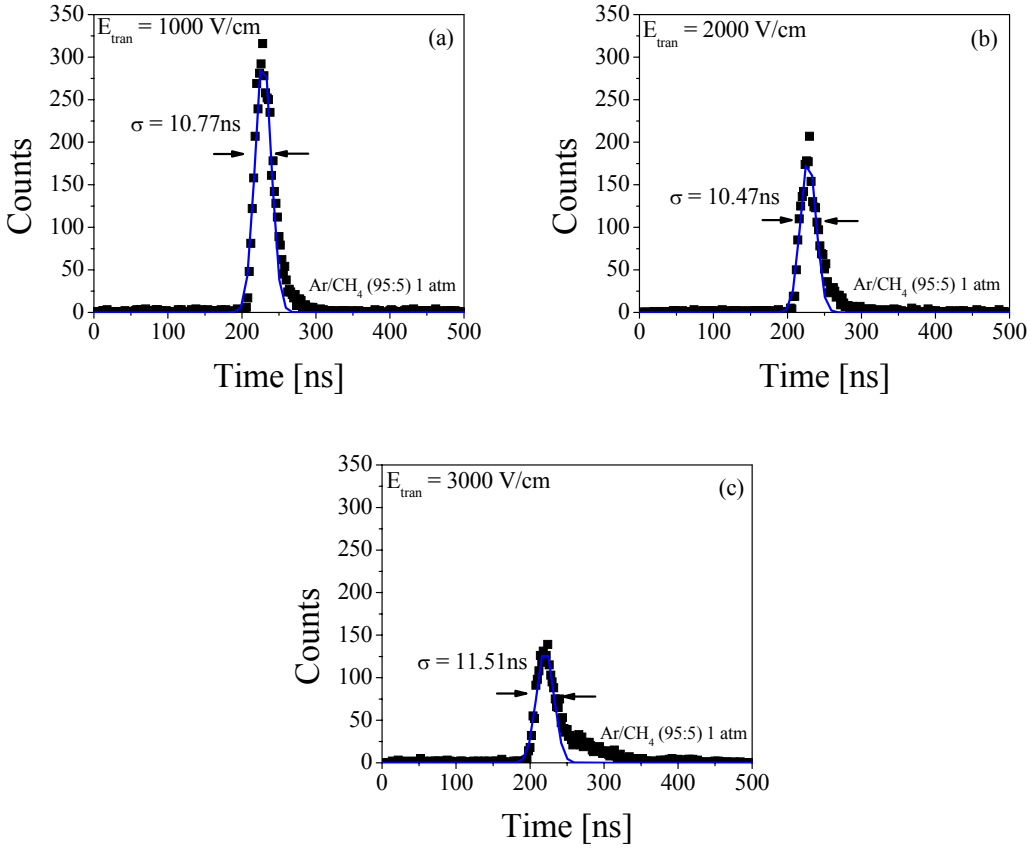

Figure 31: Time resolution at fixed drift field and CFD treshold, varying transfer field: (a) 1000 V/cm, (b) 2000 V/cm, (c) 3000 V/cm

All plots have the same scale and depict approximately the same total number of counts. The fitted RMS values have an optimum at middle-ranged fields.

The tail increases with the transfer field. This is consistent with the previous statement that it originates from low-amplitude electron-avalanche signals. The electron transfer efficiency between the two THGEMs increases with the transfer field at this range of field values [8], and thus there is more chance for events starting with a small number of primary electrons to be multiplied by both THGEMs and produce a detectable signal above threshold, which can make the difference for these events.

3.2.2.3 *Varying E_{drift}, Fixed E_{tran} and CFD Threshold, online analysis*

Figure 32 shows the time distribution at a fixed transfer field of 3000 V/cm and CFD threshold of 600 mV, for different drift fields:

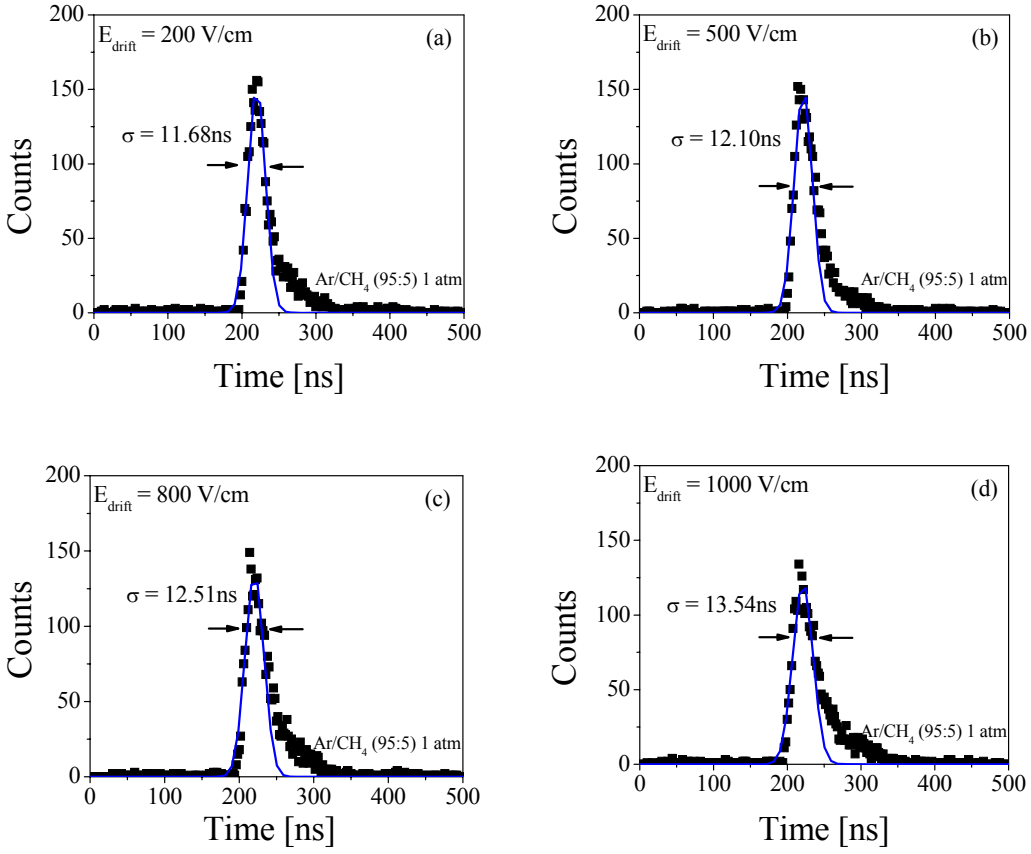

Figure 32: Time resolution at fixed transfer field and CFD threshold, varying drift field: (a) 200 V/cm, (b) 500 V/cm, (c) 800 V/cm, (d) 1000 V/cm

All plots have the same scale and depict approximately the same total number of counts. The best resolution with a fitted RMS value of 11.68ns was reached with a drift field of 200 V/cm.

3.2.2.4 ^{106}Ru Source, digital pulse shape acquisition and offline analysis

In the following results, the voltages on the THGEMs were ΔV_{THGEM1}=1220V, ΔV_{THGEM2}=1060V. The drift field was 500 V/cm while the transfer field was 3000 V/cm. A reversed induction field of –200 V/cm was applied.

Below are the results obtained while using the trigger signal from either of the PMTs separately, or the coincidence signal of the two:

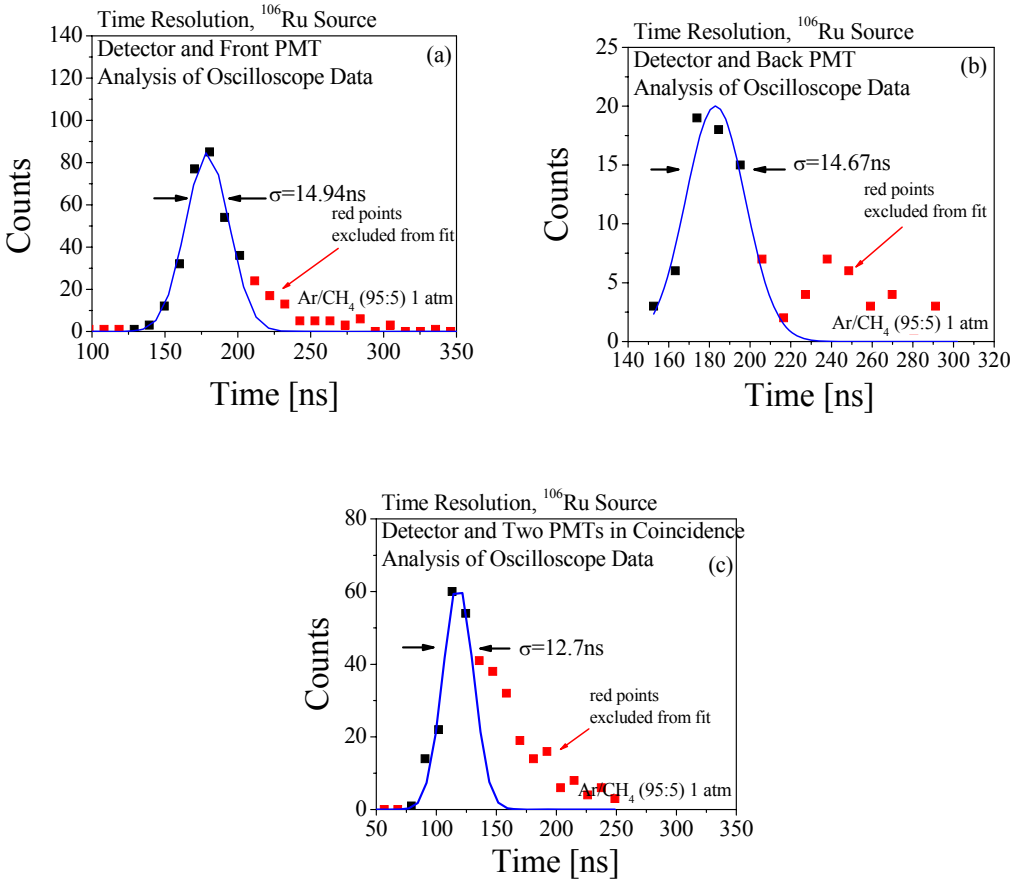

Figure 33: THGEM time resolution with the ^{106}Ru source and offline analysis. (a) Using trigger signal from the front PMT (1 in Figure 29). (b) Using trigger signal from the back PMT (3 in Figure 29). (c) Using the coincidence from both PMTs as trigger signal

Results obtained in a similar system using a triple-GEM detector and two PMTs in coincidence are shown in Figure 34. The bias on the GEMs was ΔV_1=390V, ΔV_2=380V, ΔV_3=340V. The drift field was 500 V/cm. Both transfer fields were 3000 V/cm, and the induction field was 1000 V/cm. They yielded an RMS value of 8.5ns.

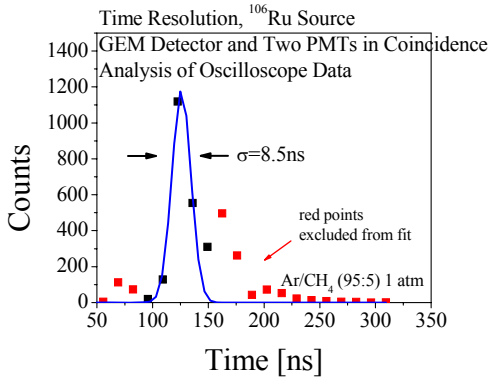

Figure 34: Time resolution using triple-GEM detector and offline analysis

In all the plots a significant tail on the right side of the peak can be observed, as in the online analysis method. An explanation was given at the end of section 3.2.2.1. A good example of the difficulty to discriminate low-detector signals resulting from low-energy deposition by the MIPs can be seen in Figure 35. On the top part, we see the signal coming out of the coincidence module. On the bottom part we see the gas detector signal. The small red circles mark the time pick-off points, which were set by the analysis program. On the left of the pick-off point in the gas detector signal there is a small peak and on the left of that peak, there is another smaller one. Either of these two can be the true primary signal, or just part of the noise.

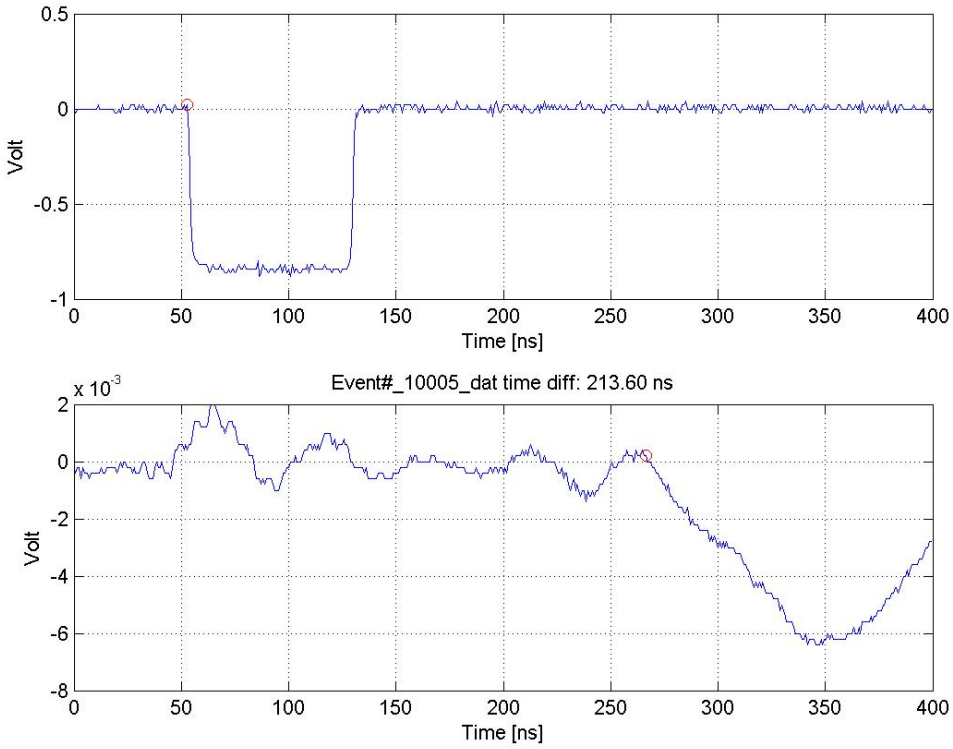

Figure 35: Typical output of the offline analysis method. Top: coincidence module signal. Bottom: detector signal. Small red circles mark the time pick-off. Notice the observable electronic noise and the similarity it may have to low-amplitude detector signals.

3.2.3 Results with Cosmic Rays

The following THGEM time-resolution results with cosmic rays were obtained with ΔV_{THGEM1}=1280V, ΔV_{THGEM2}=1090V. The drift field was 500 V/cm. Both transfer field and induction field were 3000 V/cm. For similar studies with triple-GEM, the voltages applied on the GEM electrodes were ΔV_1=400V, ΔV_2=390V, ΔV_3=350V. The drift field was 500 V/cm. Both transfer fields were 3000 V/cm and the induction field was 1000 V/cm.

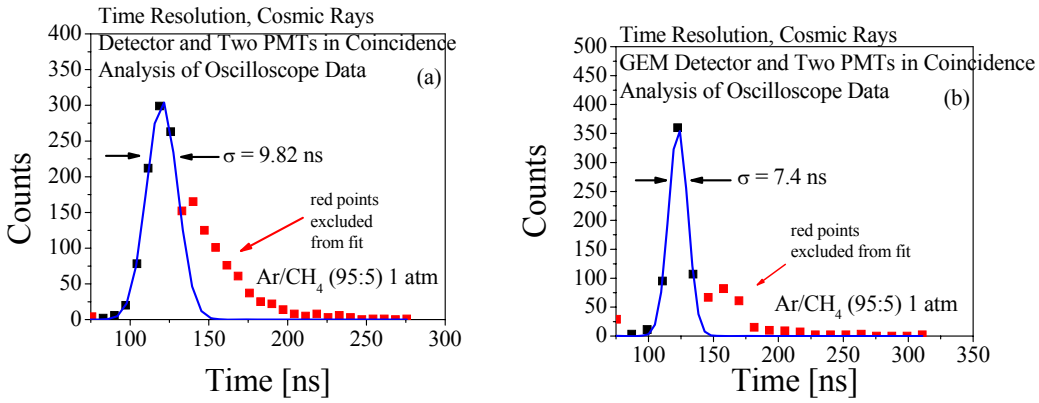

Figure 36: Time resolution with cosmic rays. (a) Double-THGEM detector, (b) Triple-GEM detector. Offline analysis was used.

3.2.4 Discussion of the time resolution with MIPs

The two analyses methods gave quite similar results, when compared at the same conditions. An RMS value of 12.1ns was measured with the online method, using a drift field of 500 V/cm and transfer field of 3000 V/cm (Figure 32 b). With the same electric field values, an RMS value of 12.7ns was obtained with the offline method (Figure 33 c). One advantage of the offline method is the ability to use digital noise filtering algorithms (not used here), which may yield cleaner data for the analysis.

A better RMS value was obtained when only the left side of the distributions was used for fitting (e.g. 7.7ns for Figure 32 b), due to the asymmetry created by the tail. This can be considered as the detector's inherent time resolution. However, it should be measured at better conditions, with mono-energetic relativistic particles, e.g. using an accelerator beam.

For both THGEM and GEM detectors, the results with cosmic rays are better than those with the β source, e.g. with double-THGEM, 9.82ns RMS obtained with cosmic rays (Figure 36 a) compared to 12.7ns RMS obtained with ^{106}Ru (Figure 33 c). When using the β source, the detector was operated with lower gain, in order to avoid sparks caused by lower-energy electrons emitted by the γ-particles of the β source. This led to inferior signal to noise and consequently worse analysis results.

Figure 32 shows that smaller drift fields yield better time resolution. The best result of 11.68ns RMS was the best time resolution obtained when the varying the drift field, for a field of 200 V/cm. As already explained earlier, this is attributed to field dependence on the drift velocity in the tested gas. On the other hand, the best time

resolution was obtained using a transfer field of 2000 V/cm (Figure 31). This is due to the balance between shortening the transfer times with lower fields, and improving the transfer efficiency with higher fields.

Figure 33 shows that as expected, the 12.7ns RMS obtained with two PMTs in coincidence is better than the 14.67ns RMS obtained with a single PMT, due to the filtration of spurious events. It is, however, worse than the result obtained with single UV photons of 10ns RMS or less, since in the latter case, all the photoelectrons are emitted from the same surface, and there is no time jitter due to conversion at different depths in the conversion gap. The only physical jitters for UV photons are due to the electron diffusion in the gas and to noise.

4. Imaging

Position-sensitive gaseous detectors are widely employed in particle physics and numerous other fields. With these, sub-millimetre localization of ionizing radiation, neutrons and soft x-rays are routinely achieved [24].

The THGEM offers an attractive alternative to current high-resolution (down to microns) gaseous detectors - in cases, which do not require very high spatial resolutions, e.g. like that of the GEM. Examples are large-area tracking detectors in particle and astroparticle physics applications, sampling elements in calorimetry, single-photon detectors in Ring-Imaging Cherenkov (RICH) detectors, neutron and x-ray inspection systems, etc.

4.1 X-Ray Imaging

4.1.1 Methodology

We investigated the imaging properties of the THGEM with soft x-rays. More details regarding the x-ray imaging detector and results are given in [11]. We investigated a 10cm x 10cm double-THGEM detector with t=0.4mm, d=0.5mm, a=1mm, having a conversion gap of 10mm, transfer gap of 2mm and induction gap of 1mm.

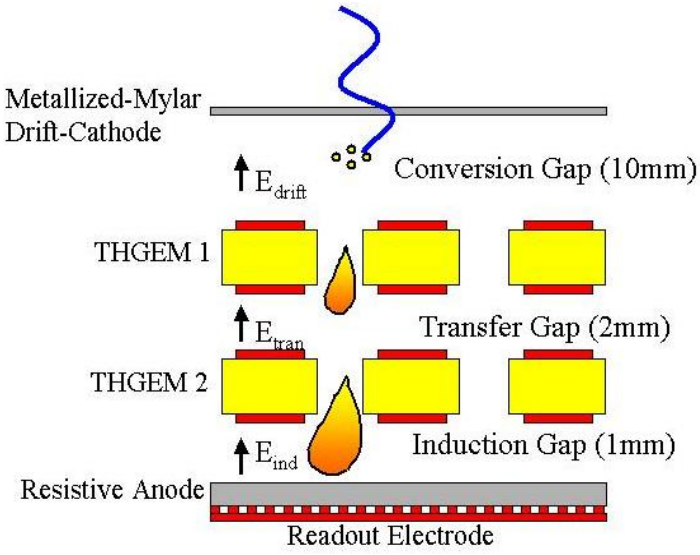

Figure 37: Schematic view of the position-sensitive THGEM detector assembly. After multiplication, the charge is collected onto a highly-resistive anode. The moving charge in the induction gap induces a localized signal at the position-encoding readout electrode.

The detector shown in Figure 37 is equipped with a resistive anode made of > 2 MΩ/square graphite lacquer layer sprayed on a G10 substrate, and a readout

electrode. The resistive anode spreads the induced signal on the readout electrode in such a way that the geometrical size of the induced charge matches the pitch of the readout circuit. This readout technique also permits for a galvanic decoupling between the multiplication stage and the readout electrode board. Therefore the resistive anode can be operated at high voltage while the readout board is kept at ground potential. The small capacitive coupling between resistive anode and readout board also protects the readout electronics from eventual spurious discharges in the detector [26].

The induced signals were collected on the double-sided X-Y readout electrode, structured with diamond-shape pads printed on both sides of a standard 0.5 mm thick printed circuit board (PCB). The pads are interconnected with strips, running in orthogonal directions (X and Y) on each of the two board faces with a pitch of 2 mm. The strips on each side of the board are coupled to a discrete delay-line circuit.

The printed diamond-shape pads are geometrically designed such that equal charge is induced on both PCB sides and they are non-overlapping in order to reduce the capacitive coupling.

The avalanche location is derived from the time difference between induced signals propagating along the discrete LC delay-line circuit. The latter is composed of 52 LC cells (Figure 38) with an inductance L=290 nH and a capacitance C=27 pF per cell; the corresponding delay is 1.4 ns/mm; the total delay for each coordinate is therefore 140 ns and the nominal impedance is of Z=103 Ω.

The readout pads were optimized for equal signal amplitudes induced on its front and back sides. The front side denotes here the one closer to the resistive anode. The copper structure on the front side causes some shielding of the board's back side to the charge moving within the induction gap. Therefore the pads on the front side have to be smaller than on the back side to allow better signal transmission. The avalanche-induced radial charge spread was fine tuned for better localization properties. A too large spread leads to broadened signals at the output of the delay lines; it causes a reduction of the signal–to-noise ratio and a deterioration of the time resolution of this encoding system. On he other hand, a radial charge spread whose full width at half maximum is narrower than the pitch of the R/O strips causes modulation of the position response by the discrete structure of the R/O board [11].

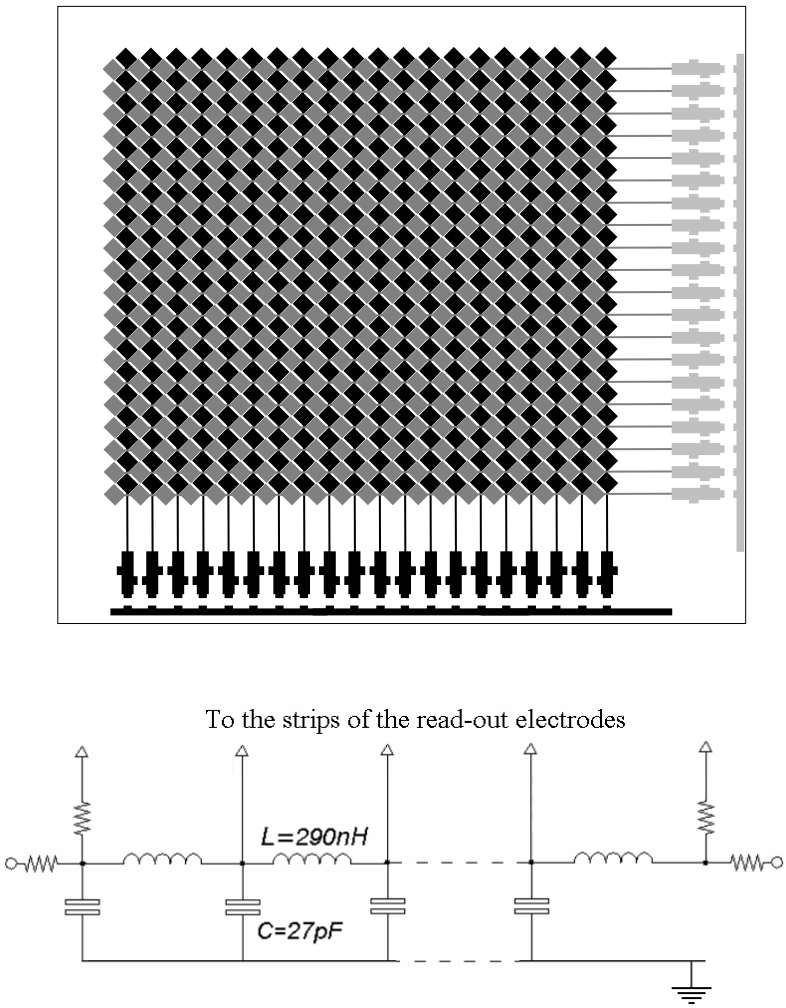

Figure 38: Schematic view of the readout electrode of the THGEM and the discrete-element LC delay-line circuit

The detector was irradiated with 6 and 8keV x-rays from a ^{55}Fe source and an x-ray generator driven Cu-fluorescence source, respectively.

Figure 39 shows the scheme of the readout electronics of the imaging detector. The data acquisition (DAQ) hardware is based on the 8 channel Time-to-Digital Converter (TDC) chip F1 and the ATMD board [27]. The system also comprises a Charge-to-Time Converter (QTC), based on LeCroy's MTQ300A-chip [28].

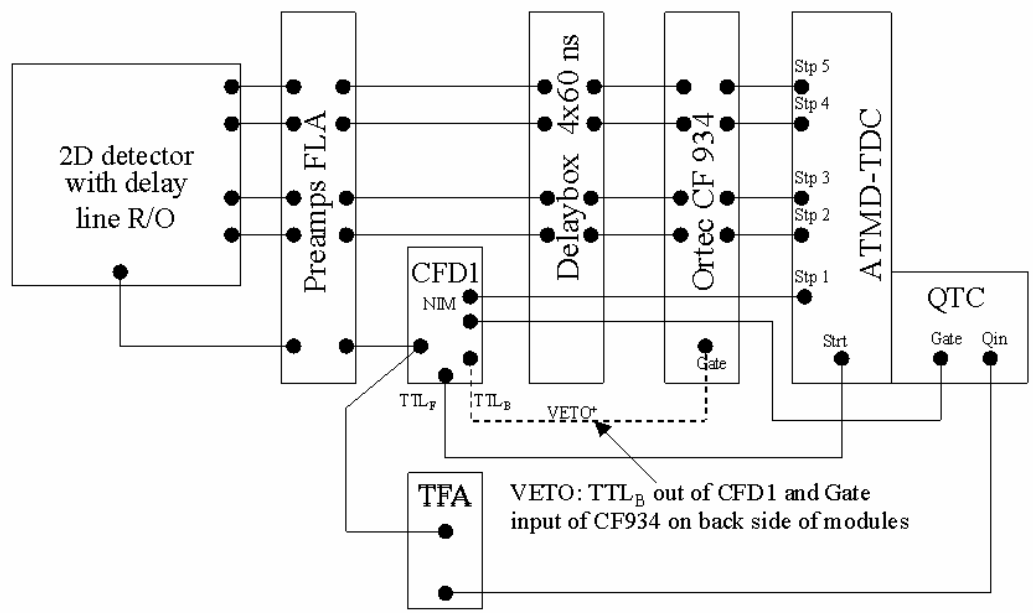

Figure 39: Schematic view of the DAQ system.

This module also permits measuring the avalanche's charge behind the last THGEM (after pulse shaping with a Timing Filter Amplifier (TFA)).

The signals from the ends of each delay-line and the common start signal from the last THGEM cathode were amplified by fast linear amplifiers (VV46, MPI-Heidelberg). The amplified position signals were delayed by 60 ns and fed to an ORTEC 934 Constant Fraction Discriminator (CFD). The common signal was discriminated by a Canberra 1428 CFD and used as common start of the TDC. The slow (TTL) output of the CFD enabled the gate of the ORTEC CFD and allowed valid signals from the delay-lines to pass. The outputs of the CFD were used as stop signals of the TDC. The data acquisition software, a modified version of CAMDA [29], calculated the position coordinates and performed a plausibility check on the measured timing signals (comparison of time-sums). Valid data were accumulated in histograms and/or stored as list-mode files in the PC memory.

The result of the digitalization process is an image of 800x800 pixels. Each pixel has a linear extension of 125 μm. The images are stored with high dynamic range (4 Byte integers per pixel).

4.1.2 Digital Noise

Electronic imaging, like all imaging techniques, is always affected by noise. The noise essentially arises due to various processes, which precede the production, capture, conversion and interpretation of the real source's signal. The quantification

of the noise is crucial for the analysis and optimization of an imaging system performance; for that reason the intrinsic signal-to-noise ratio of the imaging system was determined through the analysis of a flat-field image, obtained while irradiating the detector with a homogeneous (flat) 8 KeV photon beam. The image was recorded for 300 minutes with irradiation intensity of about 1 kHz/mm^2.

The average pixel count μ and standard deviation σ correspond to an average spread of 14% (1 standard deviation). The signal-to-noise ratio is:

$$SNR = 20\log_{10}\left(\frac{\mu}{\sigma}\right) = 16.9\,dB$$

Equation 5

The resulting digital noise is not merely due to counting statistics, which by itself would result in an average spread of 7.5% per pixel, assuming Poisson statistics. Other contributors are nonlinearities in the delay line readout (variation of the L's and C's of the delay line), cross talk of the readout channels and nonlinearities of the TDC.

The digital noise appears to be uniform across the sensitive detector area, with degradation towards the image's edges. This effect is essentially due to distortion of the electric fields near the edge of the THGEMs electrodes. Also, position sensitive gain variations in the detector lead to degradation of the general performance of the imaging system. However, image processing can largely correct these defects and restore image

4.1.3 Gain Uniformity

The gain uniformity was investigated with a collimated 5.9 keV ^{55}Fe x-ray source, 1mm^2 in diameter. The active area was irradiated in 15mm steps in both directions, for a total of 25 measurement points across the detector.

The 25 data points for ΔV_{THGEM}=1220V, the highest voltage reached at that set of measurements, had a mean gain of $6\cdot10^3$ with variation of 10% FWHM.

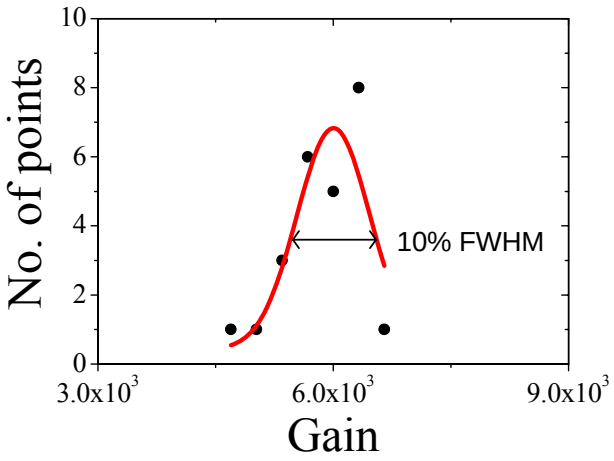

Figure 40: Gain distribution of a collimated 5.9 keV ^{55}Fe source over the sensitive area of the double-THGEM detector, measured at 25 points across its area in Ar/CH_4 (95:5); ΔV_{THGEM} = 1220V for each THGEM.

4.1.4 Imaging Linearity

The image linearity of the imaging system response was assessed by investigating the Gaussian fit of pinholes image projections. The pinholes had 1mm diameter, made on a 1mm thick brass mask (Figure 41). The detector was uniformly irradiated by characteristic K-shell fluorescence photons from a Cu- target (8 keV), which was excited by a well collimated intense bremsstrahlung-spectrum from a x-ray generator with a Mo anode.

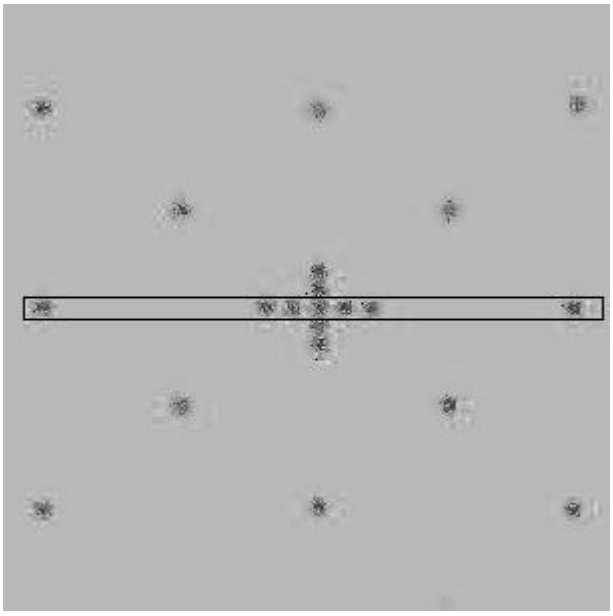

Figure 41: X-Ray transmission image of a mask with 1mm diameter pinholes, recorded with the THGEM imaging detector. The x-projected profile for INL analysis is shown

The effects induced on the image by distortions can be characterized by the integral non-linearity (INL), defined as the deviation of the measured holes' centroid from their real locations. Geometrical distortions represent a deviation from rectilinear projection (Figure 42); they may arise from several effects, such as defects on the grid cathode or signal deformation as they propagate along the delay line. Specifically, alteration of the signal shape and its rise time depend on amplitude of the signal (SNR), preamplifier cross talk, capacitive cross talk between read-out electrodes and asymmetry of induced signal on front and back. The measured average INL value is 0.02% over the full image scale of 100mm.

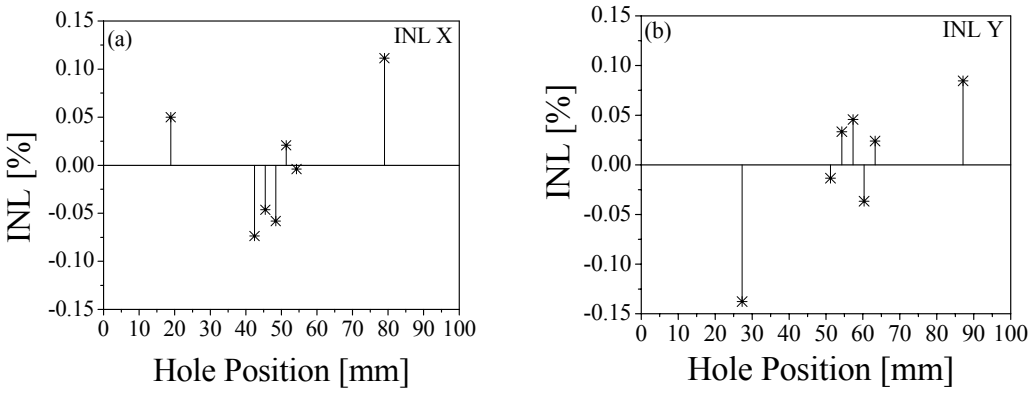

Figure 42: INL (integral non linearity) along the selected image projection along the x (a) and y (b) directions

4.1.5 Spatial Resolution

The point spread function (PSF) of the imaging detector was obtained through the edge spread function (EFS) technique [30]. The EFS was measured by irradiating the edge of a 1mm thick Aluminum plate (Figure 43 a), and extracting a projection of the edge profile from the image data (Figure 43 b).

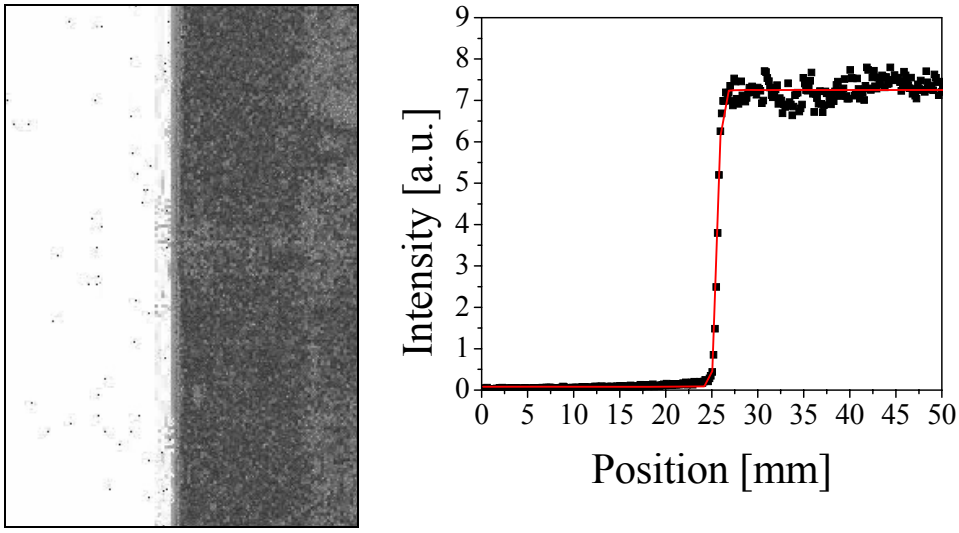

(a) (b)

Figure 43: (a) A 2D image of a knife-edge obtained with the THGEM imaging detector. (b) The edge spread function along the y coordinate. The red curve is a fit with a suitable model function

The edge profile was fitted with an empirical function, which models the ESF with adequate accuracy. The empirical model function used is given by the following equation [31]:

$$ESF(x) = a_0 + \frac{a_1}{1+\exp(-a_2(x-a_3))}$$

Equation 6

where a_0 is related to the transmission of the Al plate, a_1 is the brightness of the full irradiated sensitive area, a_2 is the steepness of the edge function (related to the spatial resolution of the imaging system) and finally a_3 is the centroid of the edge function.

The determination of the PSF was obtained in a straightforward way by simply differentiating the empirical model of the fitted ESF. Consequentially, the derived FWHM of the resulting PSF, which is a direct manifestation of the intrinsic spatial resolution of the system, is then given by:

$$FWHM = 2\frac{\operatorname{arcosh}(3)}{a_2}$$

Equation 7

To check the consistency of the estimate of the spatial resolution, the PSF and its FWHM were determined by two different methods: from numerical differentiation of the measured ESF data, followed by a Gaussian fit, and the differentiation of the suggested empirical model. There is good agreement between the methods.

Nevertheless the direct analysis of the raw data, fitted with a Gaussian function distribution, has large fluctuations due to the digital noise; the related Gaussian fitting, and the resultant spatial resolution, has a larger error.

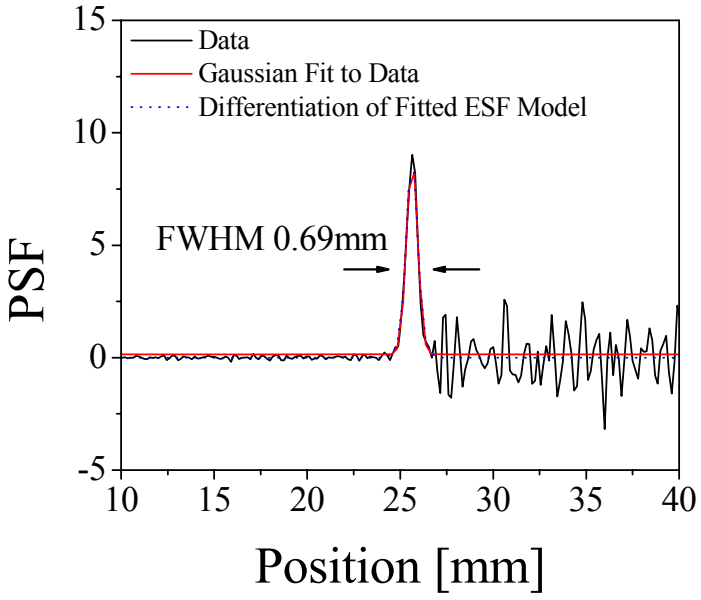

Figure 44: Results of the PSF determination along the y-coordinate using the differentiation of raw data (black line), its fitted Gaussian (red line), and the differentiation of the empirical model (blue line)

The spatial resolution obtained through the "measured" PSF, from raw data analysis, has a FWHM value of 0.69±0.02mm, while the empirical model analysis reveals a FWHM value of 0.68±0.03mm.

4.2 Neutron Imaging

The interaction cross sections of fast neutrons (with energies greater than 0.1 MeV) with matter have an isotope-specific resonant structure. This has led to the development of element-specific fast-neutron radiography and tomography methods [32]. In these methods, an object is illuminated by a pulsed neutron beam of a broad energy distribution (0.8 – 10 MeV). The energy spectrum transmitted through the object is modified due to the resonant features in the cross-section of the object's elements. The transmitted energy is measured using the time-of-flight technique. This method has been applied for detection of elements such as C, O, N and H for determining the composition of agricultural products, for detecting contraband, and for detecting explosives [32].

The possibility of performing fast-neutrons resonant transmission (FNRT) imaging and spectroscopy was investigated using the neutron beam facility at PTB-Braunschweig. In this facility, neutrons are produced by a nanosecond pulsed deuterium beam hitting a thick Be target. Two different imaging detectors were developed. One is based on a thin hydrogenous neutron converter foil (e.g. polyethylene) coupled to a GEM-based gaseous detector. The second one is based on a fast plastic-scintillator screen viewed by gated intensified CCD cameras [32].

In this work we carried out a first preliminary study of a THGEM-based neutron detector, as an alternative for the GEMs presently in use. Unfortunately, due to short supply of detector parts and limited allocated beam-time, no conclusive results were obtained and this research is currently pursued with better-quality detector elements.

4.2.1 Methodology

The neutron imaging detector was similar the x-ray imaging detector described above. The conversion gap was reduced to 1.8mm. A hydrogen rich neutron converter foil (radiator) was installed in front of a double-THGEM. In this foil neutrons are converted into protons, which can escape from the foil surface and ionize the gas in the conversion gap through Coulomb interaction.

The physical mechanism behind the conversion of fast neutrons into protons is elastic neutron scattering with hydrogen nuclei, in which an incident neutron transfer a portion of its kinetic energy to the proton, thus producing a recoil nucleus. The scattering nucleus then gains energy given by [12]:

$$E_R = \frac{4A}{(1+A)^2}(\cos^2\theta)E_n$$

Equation 8

Where (all symbols are in the lab system) E_R is the recoil nucleus kinetic energy, A is the ratio of target nucleus mass to neutron mass, θ is the scattering angle of the recoil nucleus, and E_n is the incoming neutron kinetic energy. Hydrogen is a favorable scatterer since as seen in Equation 8 for A=1, the recoil proton resulting from the collision can gain energy up to the full energy of the incoming neutron. Moreover, the cross section for neutron elastic scattering from hydrogen is large and its energy dependence is accurately known [12].

The neutron-radiator thickness was optimized to satisfy two conflicting requirements: The converter should be sufficiently thick to efficiently convert the incident neutron

flux, and sufficiently thin to permit the efficient escape of the resulting charged particles into the detector's gas. This last requirement favors thin radiators, and reactions yielding light charged particles of highest possible kinetic energy, which again favors hydrogen as converter material.

Furthermore, materials of low stopping power (dE/dx) are preferable [33, 34]. A 1mm thick polypropylene radiator was used, coated with a thin layer of graphite in order to act as the drift electrode. Polypropylene (and also polyethylene) have excellent properties as radiators because they are rich in hydrogen and have comparably low dE/dx. The detector scheme is shown in Figure 45.

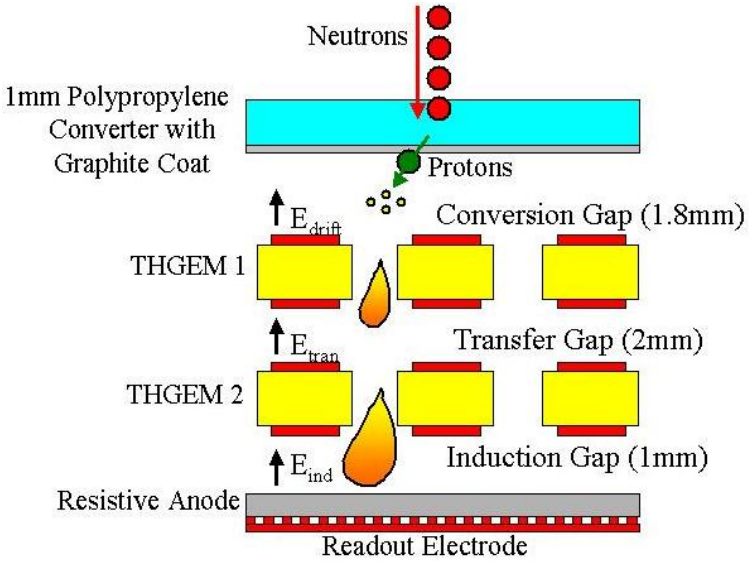

Figure 45: Scheme of the neutron imaging detector.

The readout electronics (Figure 46) was altered in comparison to that of the x-ray imaging detector described above. PTB-made dedicated preamplifiers were installed inside the detector's vessel to reduce electronic noise.

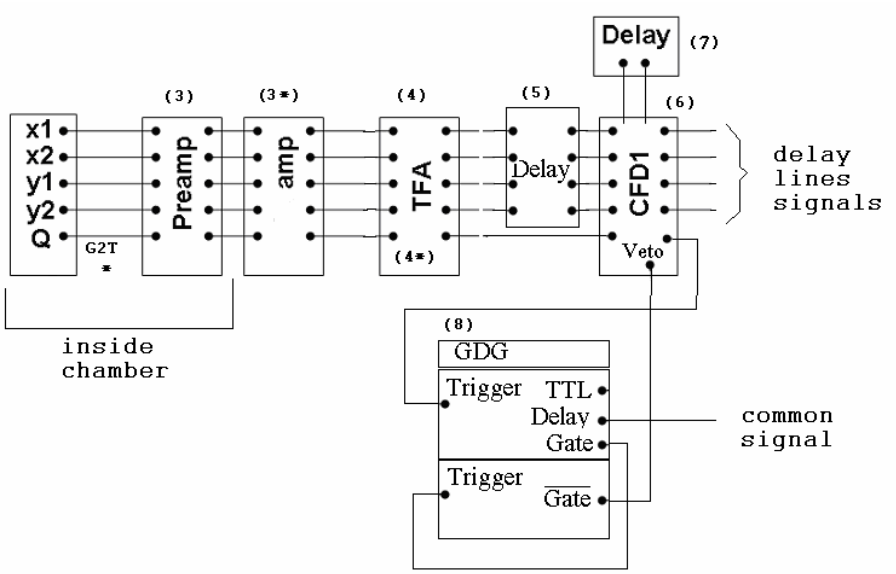

Figure 46: Schematic view of the DAQ system in the neutron beam room.

The modules used:

(3) PTB made preamplifier (inside vessel)

(3*) PTB made amplifier (outside vessel)

(4) ORTEC 474 Timing Filter Amplifier (TFA)

(4*) ORTEC 454 TFA

(6) Phillips Scientific (P/S) 715 Constant Fraction Timing Discriminator (CFD)

(7) Phillips 794 Gate/Delay Generator (GDG)

Due to the long cables running from the experiment room up to the control room, the digital signals were reprocessed as seen in Figure 47.

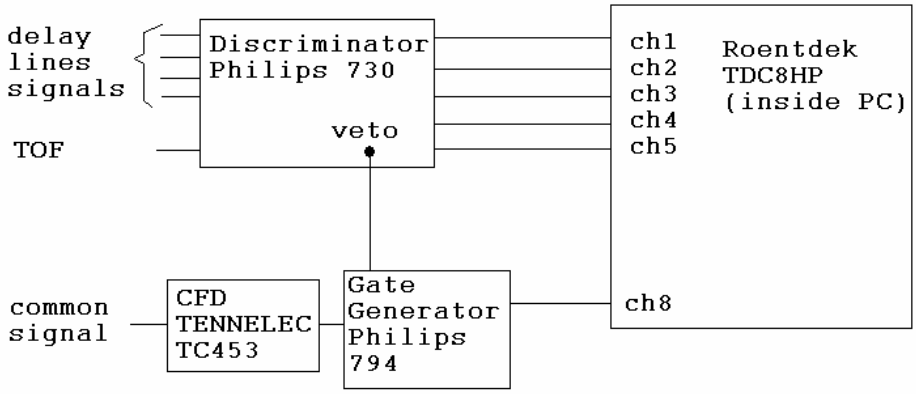

Figure 47: Electronics setup in control room

The specific THGEM detector tested at PTB suffered from technical problems. The first pair of THGEMs were previously used for other measurements, and sparks

occurred at specific hot-spots on the electrodes, up to a point which prevented further work. A newer pair was then installed in the detector. However, in polypropylene neutrons also produce recoils of heavier Z, e.g. carbon, which sometimes are also emitted into the gas or produced in the conversion gap. These slow heavy ions have very high dE/dx and thus produce high ionization densities in the conversion gap. This regularly leads to electric discharges at higher gains, which are required for the detection of the protons. Therefore, the detector was operated at lower gain to avoid damaging the electrodes. Consequently, each measurement yielded images with relatively low pixel-count and thus bad statistics.

4.2.2 Digital Image-Correction Algorithms

Three image-correction algorithms were investigated:

1. Flat field correction, obtained by dividing the image, pixel by pixel by the flat image (broad beam detector illumination without objects).
2. Dark image subtraction (dark image is an image taken without external irradiation):

   We define the following three values:

   F1 = image exposure time / dark image exposure time

   F2 = flat image exposure time / dark image exposure time

   F3 = image exposure time / flat image exposure time

   The corrected image is then given by:

$$\text{corrected image} = \frac{\text{image} - \text{F1} \times \text{dark image}}{(\text{flat image} - \text{F2} \times \text{dark image}) \times \text{F3}}$$

Equation 9

3. We define the following two values:

   Npix = number of pixels in flat image with count > threshold

   PixSum = sum of counts for all pixels in flat image with count > threshold

   After setting all pixels in flat image with count < threshold to have the value of 1 count, the corrected image is given by:

$$\text{corrected image} = \frac{\text{image}}{\text{flat image} \times \frac{\text{NPix}}{\text{PixSum}}}$$

Equation 10

4.2.3 Digital Noise

As with the x-ray imaging detector (see section 4.1.2), an image of a flat field was taken, and the signal to noise ratio measured was

$$SNR = 20\log_{10}\left(\frac{\mu}{\sigma}\right) = 20\log_{10}\left(\frac{50.37}{9.35}\right) = 14.63\,dB$$

Equation 11

4.2.4 General Image Quality

Figure 48 is a greyscale version of the flat-field image. Notice the dark region with lower pixel-count near the top right corner, marked with a circle (the axes are in arbitrary units).

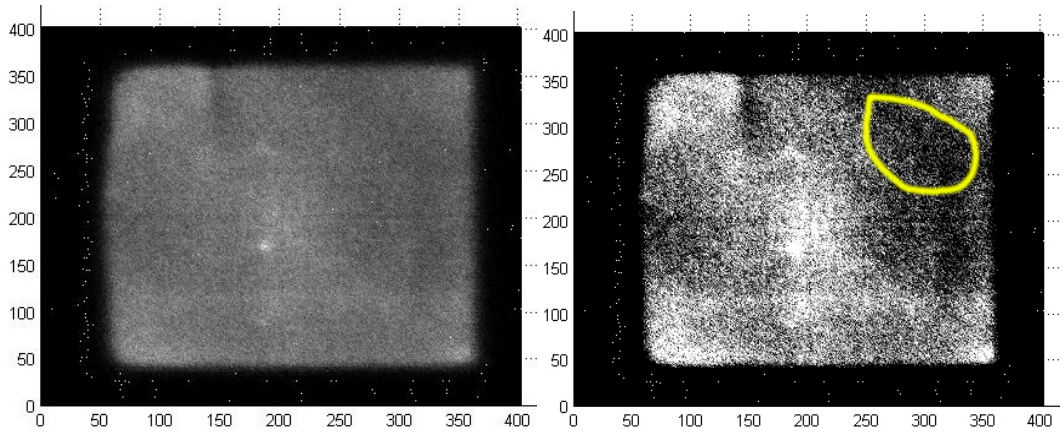

(a) (b)

Figure 48: The flat-field image (a); and the same image with enhanced contrast (b) A lower pixel-count region is marked.

An image of a small water-filled plastic vial, and a steel pocket knife was taken as shown in the setup in Figure 49

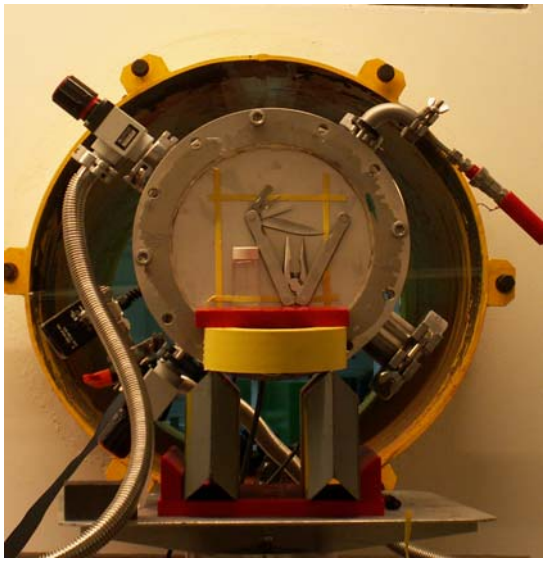

Figure 49: Picture of water filled plastic vial and pocket knife, placed in front of the detector's vessel in the beam room

Figure 50 is a greyscale version of the raw image, and an enhanced contrast version of it (the axes are in arbitrary units).

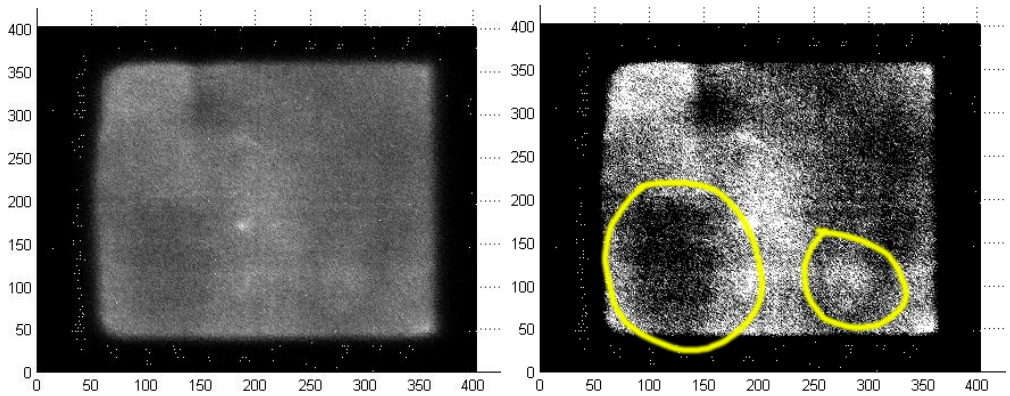

Figure 50: Raw image of the objects shown in Figure 49 (a); and the same image with enhanced contrast (b) Structures of the water vial and possibly of the pocket knife are marked.

In comparison with Figure 49, the water vial is slightly visible on the bottom left part of the image. Some structures are visible at the bottom of the pocket knife, as well as at its top left hand. However, the rest of the darker areas can be attributed to the same areas in the flat image, as seen in Figure 48.

Good statistics would permit extracting of the objects image by dividing the raw image by the flat image, pixel by pixel. However, due to bad statistics, this was not practiced here.

4.2.5 Spatial Resolution

The result of imaging a mask with a rectangular transmission profile at different fundamental frequencies is a frequency-dependent variation of the modulation depth (Contrast Transmission) in the images [35]. The contrast transfer function (CTF) approaches a value of 100% at very low spatial frequencies, corresponding to a wide spacing period, and gradually drops with increasing spatial frequency. In general, 100% contrast represents regular white and black repeating bars, while 0% contrast is manifested by grey bars that mix into a grey background of the same intensity. After the contrast value reaches zero, the image becomes uniformly grey, and remains as such for all higher spatial frequencies.

The specimen modulation (contrast), *M(v)*, for patterns at different frequencies, can be defined as

$$M(\nu) = \frac{I(\max) - I(\min)}{I(\max) + I(\min)}$$

Equation 12

where *v* is the spatial frequency of the grating specimen, *I(max)* is the maximum intensity transmitted by a periodic structure (grating) and *I(min)* is its minimum intensity. The CTF is defined as the modulation depth of the image (M_i) divided by the modulation depth of the stimulus (M_o),

$$CTF(\nu) = \frac{M_i(\nu)}{M_0(\nu)}$$

Equation 13

The CTF is normalized to unity at the lowest spatial frequency, at which the imaging system yields the maximal transfer contrast.

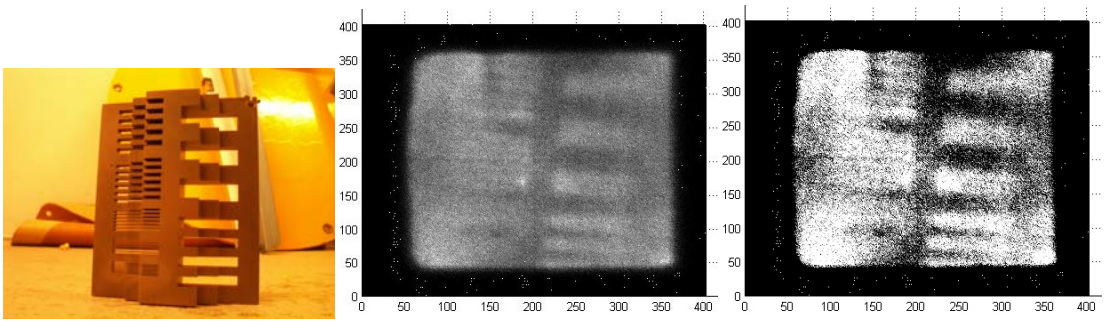

(a) (b) (c)

Figure 51: (a) The tungsten mask used for measuring spatial resolution of the THGEM detector; (b) The raw mask image; (c) Mask image with enhanced contrast

The methodology for measuring the detector's resolution using a tungsten mask was as following:

a) The mask image was rotated in order to align it to the x/y axes.
b) The image was digitally corrected using either of algorithms described in section 4.2.2.
c) Two rectangular profiles of the low and high frequency areas of the image were taken, along the thickest part of the mask.
d) From these profiles, the modulation was deduced.
e) The CTF was calculated by normalizing the modulation by that of the lowest frequency.
f) Two more data points were artificially added: CTF(0) = 1 and CTF(1) = 0.
g) CTF was fitted with a double Gaussian model: $y = a_0 e^{-(a_1 x)^2/2} + (1 - a_0) e^{-(a_2 x)^2/2}$ [36].
h) Using the Coltman formula [36, 37], the CTF was converted to MTF.
i) The PSF was calculated as the inverse Fourier transform of the MTF.

The resolution was set as the FWHM of the PSF.

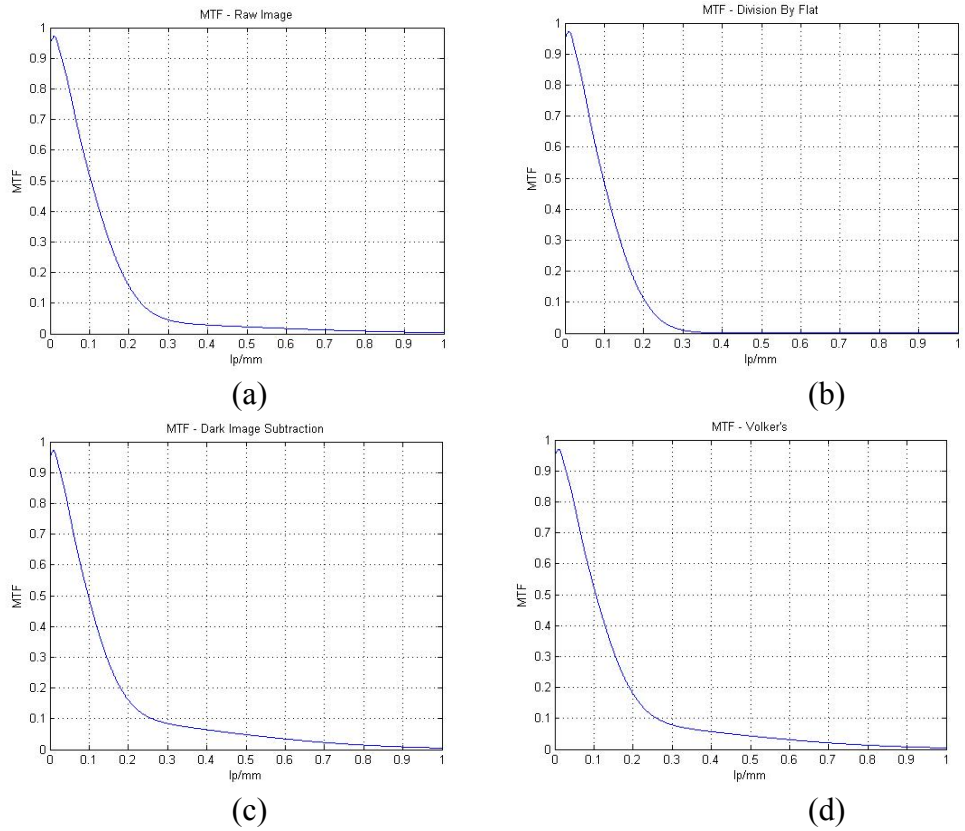

Figure 52: The measured MTF using different image correction algorithms from section 4.2.2: (a) no algorithm, (b) algorithm 1, (c) algorithm 2, (d) algorithm 3

The plots are quite similar. Except for the simple flat image division case, the curves cross the 5% line at around 0.4 – 0.5 lp/mm.

Table 2 summarizes the FWHM values of the resulting PSF. The FWHM value was divided by 2 for conversion from line pairs to single lines:

Image	FWHM (mm)
Raw Image	1.36
Algorithm 1	1.67
Algorithm 2	1.12
Algorithm 3	1.15

Table 2: Spatial Resolution – PSF FWHM

The simple division by flat image yielded a worse resolution than the raw image. This may be attributed to bad statistics.

Inspecting the images visually, the 1mm wide grooves in the mask were always unresolved, while the 2mm wide grooves could be resolved. This means that the "visual" resolution (objects which one can resolve visually) is between 1mm and 2mm, which fits the limit spatial resolution, even though their definitions are not the same (one may visually resolve objects which are smaller than the limit spatial resolution).

5. Operation in Ar, Xe and Ar/Xe

This part summarizes the work of a joint effort of all the authors of ref. [38].

The development of novel detectors, having high sensitivity to rare events, with low radioactive background, low energy threshold, and a large mass at a low cost, is crucial for carrying out advanced research in the fields of neutrino, double-beta decay and dark-matter physics [39-45].

There has been a growing interest in utilization of double-phase radiation detectors in these fields [46-50]. In such devices, the incoming particle interacts with a noble liquid, creating ionization electrons which are extracted under electric field into the gas phase and detected after proportional scintillation or gas-avalanche multiplication. In addition, the prompt scintillation of noble liquids can be exploited as well; the scintillation photons may be detected with vacuum photomultipliers in or above the liquid [44], or with gaseous photomultipliers equipped with a photocathode (e.g. CsI [51]). The scintillation photons can be also detected with a photocathode immersed within the noble liquid [52]; here the resulting photoelectrons are extracted from the liquid into the gas phase and detected similarly to the ionization electrons, as described above. Alternately, the ionization electrons and the photoelectrons can also be detected with gaseous photon detectors that record the secondary scintillation light emitted during their transport in the gas phase under high electric fields [53, 54].

In recent years there have been numerous works describing possible solutions to the detection of charges in the gas phase of noble liquids. Some use avalanche multiplication in discrete holes, as to reduce to a minimum secondary effects due to avalanche-induced photons; others use secondary scintillation, induced by electrons drifting in the gas phase, detected by photomultipliers [44]. In charge-multiplication mode, cascaded GEMs, with holes approximately 50 microns in diameter, were shown to operate in noble gases at cryogenic temperatures, including in two-phase conditions [48, 49, 55]; their limited gain could have resulted from condensation of the very cold gas within the tiny holes. There have been other suggestions of using "optimized GEM" multipliers [56], "Large Electron Multipliers" (LEM) [57], MICROMEGAS [58] and more recently Resistive Thick GEMs (RTHGEM) [59].

These have millimeter-scale diameter holes drilled in millimeter-scale thick insulator materials.

This work describes the operation properties in noble gases of the THGEM. These electrodes can be manufactured from many different substrate materials. In particular Cirlex (polyimide) with low natural radioactive background [60].

In this work results presented of recent studies conducted on the operation of THGEM-based detectors in 1 bar Ar, 0.5-2.9 bar Xe and in the Penning mixture of 1 bar Ar/Xe (95:5) [61, 62] at room temperature. Gain and energy resolution were measured for THGEM electrodes of various geometrical parameters in various detector configurations. The experimental research was accompanied by simulation studies.

5.1 Methodology

Measurements were carried out with single-THGEM and double-THGEM detector configurations (Figure 3). The THGEM electrode geometries employed in this work are summarized in Table 3.

Thickness (mm)	Hole Diameter (mm)	Pitch (mm)	Gas	Detector configuration
0.4	0.3 0.5 0.6 0.8	0.8 0.9 1.2 1.3	Argon	Single
	0.3	1.0	Xenon	Single/ Double
	0.5	0.9	Ar/Xe (95:5)	Single/ Double
0.8	0.4 0.6 0.8	0.9 1.2 1.3	Argon	Single
	0.4	1.2	Xenon	Single/ Double

Table 3: THGEM geometries, gases and configurations investigated in this work

Measurements in Ar were done under continuous gas flow or in a closed vessel. In Xe and in Ar/Xe (95:5), the chamber and the gas system were pumped down to ~10^{-5} mbar by a turbo-molecular pump, and then filled with gas at different pressures (without baking); in this closed system, the gas purity was maintained by convection-induced circulation through non-evaporable getters (SAES St 707). The latter, kept at ~200-250^{o}C, were enclosed in a small annex tube connected directly to the chamber. The detector was irradiated with x-rays originating from ^{55}Fe (5.9 keV) and ^{109}Cd (22.1 keV) sources.

5.2 Gain

Figure 53 shows typical gain curves measured in 1 bar Ar, Ar/Xe (95:5) and Xe in double-THGEM detectors having thicknesses of 0.4 mm and hole diameters of 0.3, 0.4 and 0.5 mm, in a closed system. The maximum effective charge gains reported correspond to the appearance of discharges or spontaneous electron emission. In Xe and Ar/Xe (95:5), the maximum gains reached with two cascaded THGEMs, with optimized drift-, transfer- and induction-fields [8], were above 10^4 at atmospheric pressure. Ar measurements in a closed system (Figure 53) yielded lower gain than those taken in gas-flow mode (see Figure 54 and discussion below).

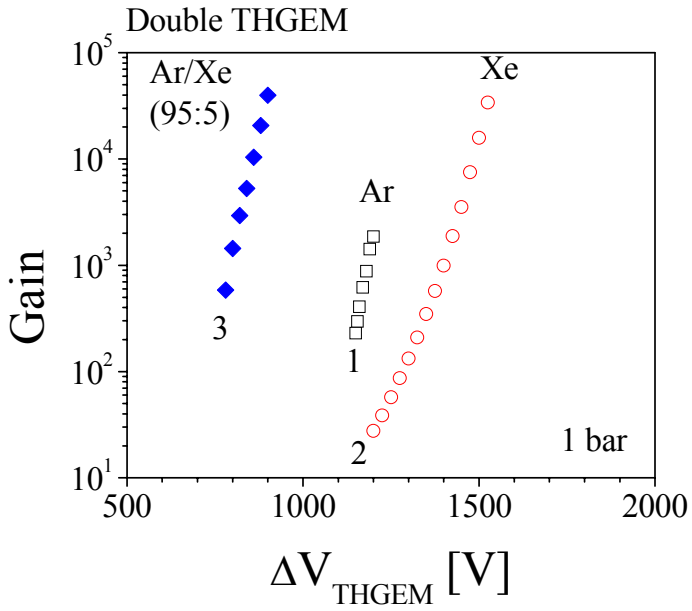

Figure 53: Gain curves of a double-THGEM operated in a closed system, with internal gas circulation through a getter after evacuation to high vacuum: (1) Ar: t=0.4mm, d=0.5mm, a=0.9mm; (2) Xe: t=0.4mm, d=0.3mm, a=1mm and (3) Ar/Xe (95:5): t=0.4mm, d=0.5mm, a=0.9mm.

Unless otherwise mentioned, all the following measurements in Ar were done in a gas-flow mode.

Different THGEM-electrode geometries were investigated in 1 bar Ar, as shown in Figure 54. In terms of gain, they all provided rather similar results, except for one, in which the diameter was twice as large as the electrode's thickness (curve 5 in Figure 54). As pointed out in [8], maximal gain is typically reached when the ratio t/d ~1. Curve 5 should be compared to curve 8 in Figure 54, which was measured with the same hole diameter and pitch but twice the thickness.

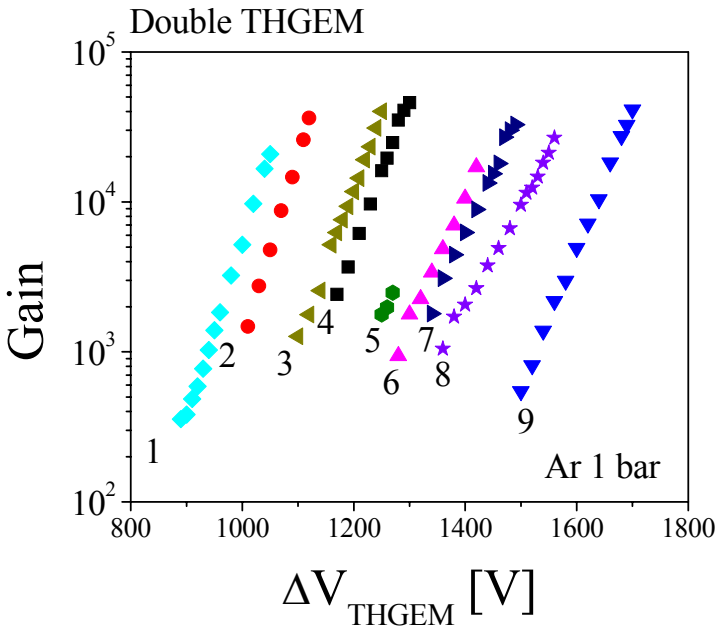

Figure 54: Double-THGEM gain curves measured with 5.9keV x-rays in various geometries in Ar, in a gas-flow mode at 1 bar: (1) t=0.4mm, d=0.3mm, a=0.7mm; (2) t=0.4mm, d=0.3mm, a=0.8mm; (3) t=0.4mm, d=0.5mm, a=0.9mm; (4) t=0.4mm, d=0.6mm, a=1.2mm; (5) t=0.4mm, d=0.8mm, a=1.3mm; (6) t=0.8mm, d=0.4mm, a=0.9mm; (7) t=0.8mm, d=0.6mm, a=1.2mm; (8) t=0.8mm, d=0.8mm, a=1.3mm; (9) t=0.8mm, d=0.6mm, a=1mm

In the Xe measurements, the electric fields in the different gaps were increased with pressure in order to maintain constant reduced electric field (E/p) values. Within the THGEM's holes, the E/p values were limited by the maximum voltage the THGEM could hold. This resulted in a continuous decrease in the maximum reachable gain with pressure increase. The results for single- and double-THGEMs with electrode thicknesses of 0.4 and 0.8 mm are shown in Figure 55.

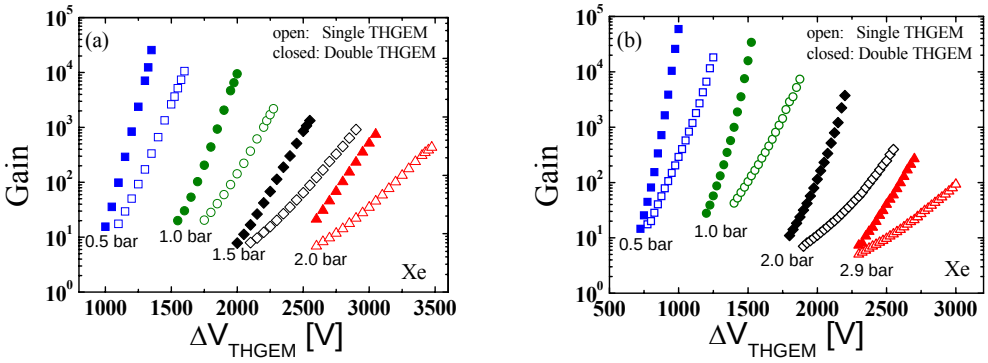

Figure 55: Gain curves in single- and double-THGEM operated in Xe at various pressures: (a) t=0.8mm, d=0.4mm, a=1.2mm; (b) t=0.4mm, d=0.3mm, a=1mm. Measurements at pressures of 0.5 and 1 bar were done with 5.9 keV x-rays and with 22.1 keV x-rays at pressures above 1 bar.

Figure 56 shows gain curves measured with single- and double-THGEMs in the Ar/Xe (95:5) mixture at 1 bar, in a closed vessel after evacuation to high vacuum. A gain curve in 1 bar Ar, measured with the same detector in similar conditions, is shown for comparison.

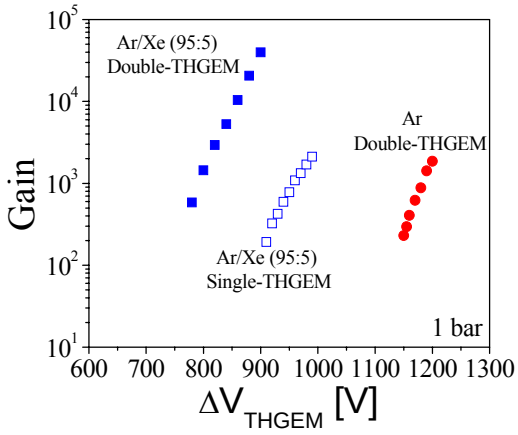

Figure 56: Gain curves in single- and double-THGEM operated in Ar/Xe (95:5) at1 bar, in a closed vessel with internal gas circulation through a getter. The gain curve in Ar, measured with the same THGEM electrodes and in the same conditions is shown for comparison. Detector parameters: t=0.4mm, d=0.5mm, a=0.9mm.

Figure 57 shows gain curves measured with a double-THGEM detector in Ar/Xe (95:5) in a pressure range of 0.1-2 bar. The measurements were done in a closed vessel, after evacuation to high vacuum.

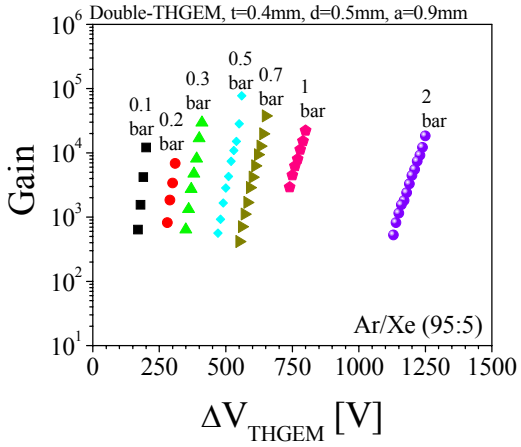

Figure 57: Gain curves taken in Ar/Xe (95:5) with a double-THGEM detector in different pressures as indicated in the figure. Detector geometry is shown in the figure.

5.3 Energy Resolution

Pulse-height spectra recorded in Ar and Xe in different THGEM configurations, with ^{55}Fe and ^{109}Cd x-rays are shown in Figure 58. Figure 59 shows pulse-height spectra recorded in Ar/Xe (95:5) with ^{55}Fe 5.9 keV x-rays.

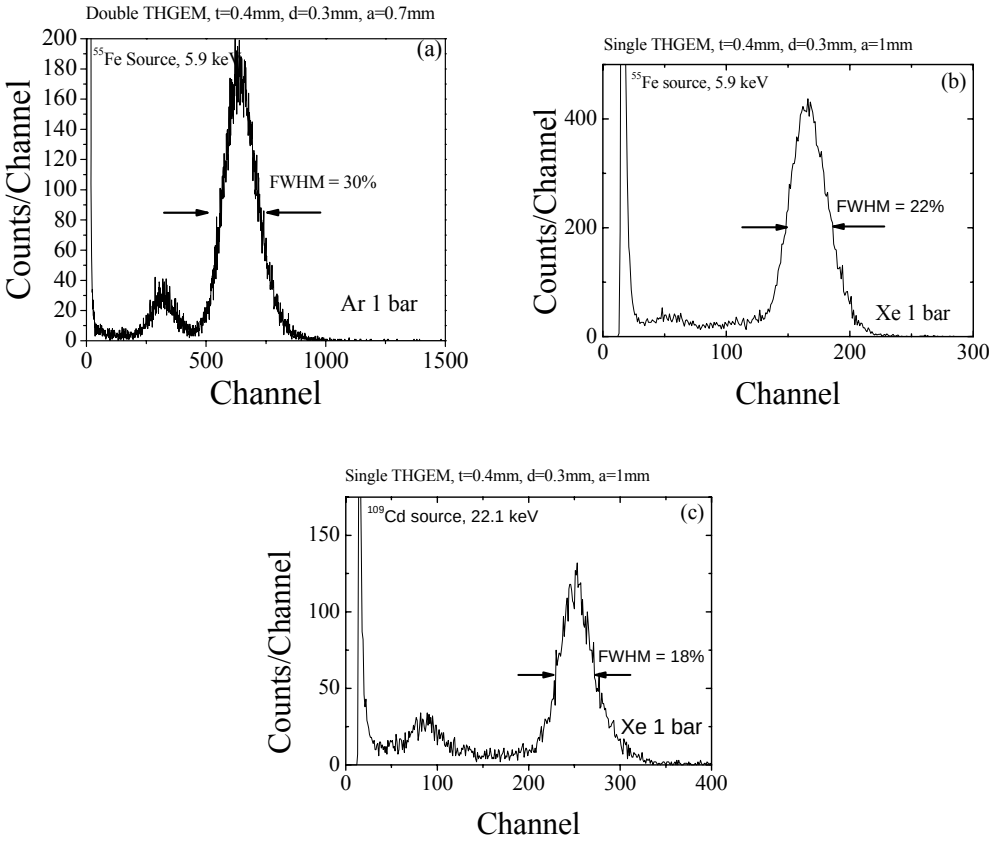

Figure 58: Pulse-height spectra recorded in single- and double-THGEM detectors of geometries indicated in the figures, at 1 bar in: Ar (a) and Xe (b), with ^{55}Fe 5.9 keV x-rays and Xe (c) with ^{109}Cd 22.1keV x-rays, for detector gains ~10^3 and ~10^4 in single- and double-THGEM respectively.

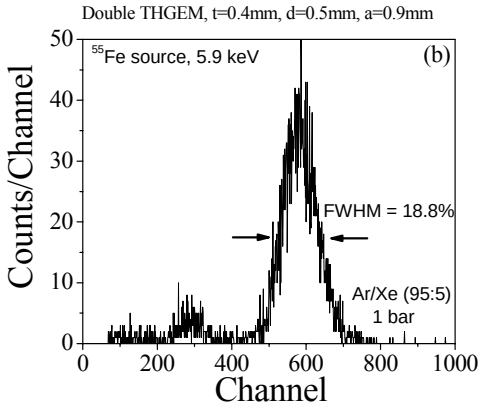

Figure 59: Pulse-height spectra recorded with a double-THGEM detector of geometry indicated in the figure, at 1 bar Ar/Xe (95:5) with ^{55}Fe 5.9 keV x-rays. Detector gain ~10^4.

The energy resolution is known to depend on the drift field, which defines the electron diffusion. With hole multipliers, the resolution is first and foremost defined by the ratio of drift-to-hole fields, since this field ratio defines the electron transfer efficiency, namely the efficiency to bring a single electron from the drift gap into the multiplication region inside the hole. This ratio should not be too large or the electron will be collected at the metal top (cathode) face of the THGEM. The dependence on the drift field is shown in Figure 60 for Xe with 5.9 keV and 22.1 keV x-rays, and in Figure 61 for Ar with 5.9 keV x-rays. At fixed gain (hole field), the resolution indeed deteriorates, and more pronouncedly so with the smaller hole diameter.

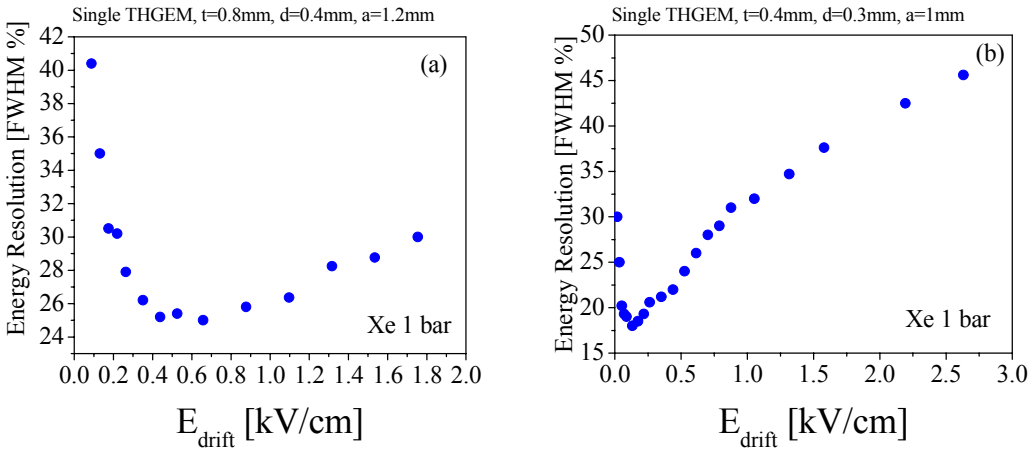

Figure 60: Energy resolution of a single-THGEM versus drift field, measured in 1 bar Xe: (a) 5.9 keV x-rays, t=0.8mm, d=0.4mm, a=1.2mm; (b) 22.1 keV x-rays, t=0.4mm, d=0.3mm, a=1mm. Detector gain ~10^3

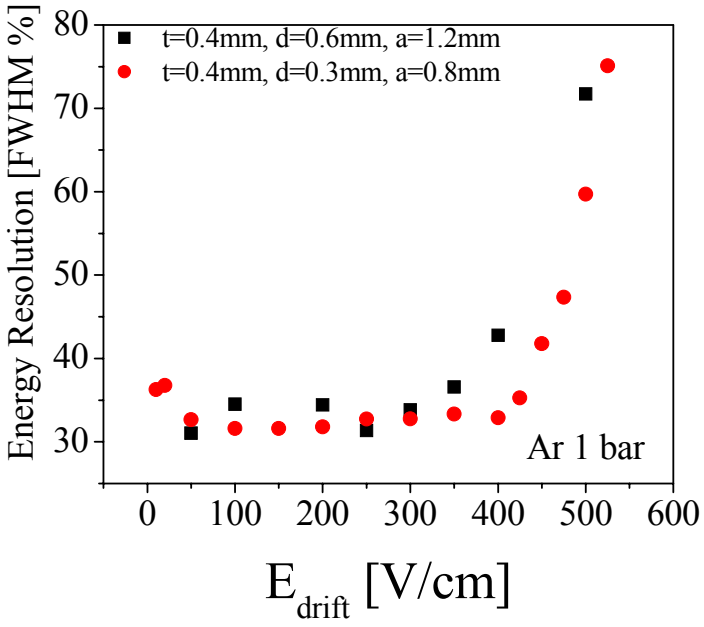

Figure 61: Energy resolution versus drift field in a double-THGEM operated with 5.9 keV x-rays in 1 bar Ar. Detector gain ~10^4

In full agreement with the above mentioned electron transfer efficiency dependence on the drift-to-hole field ratio, an improvement of the energy resolution with gain increase, up to gain values of the order of ~10^4 was measured in Ar (Figure 62); this occurred for various values of the drift field.

The curves of the energy resolution versus gain in Ar/Xe (95:5) have similar shapes to those measured in Ar; however, with better energy resolution, as shown in Figure 63.

Figure 64 shows the best energy resolution obtained in Ar/Xe (95:5) over a pressure range of 0.4 to 2 bar.

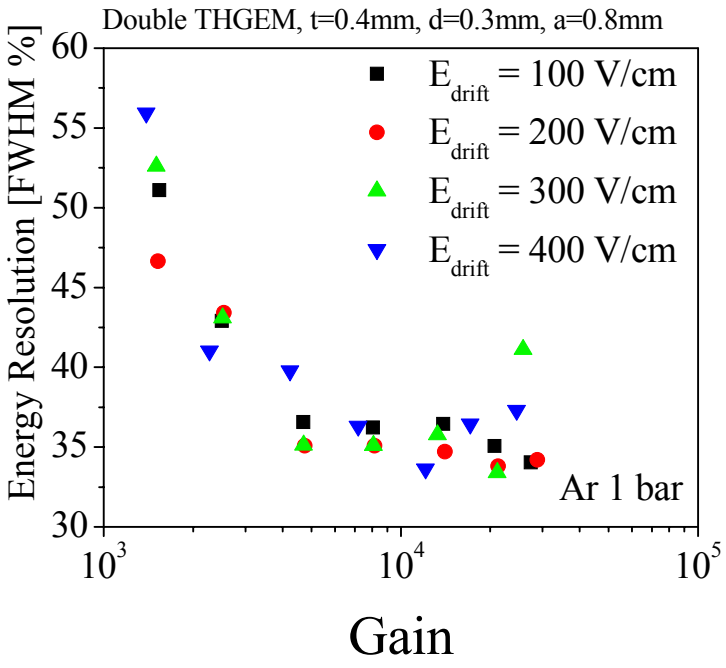

Figure 62: Energy resolution versus gain in a double-THGEM detector operated in a gas-flow mode in 1 bar Ar, at different drift fields. Detector parameters are shown in the figure.

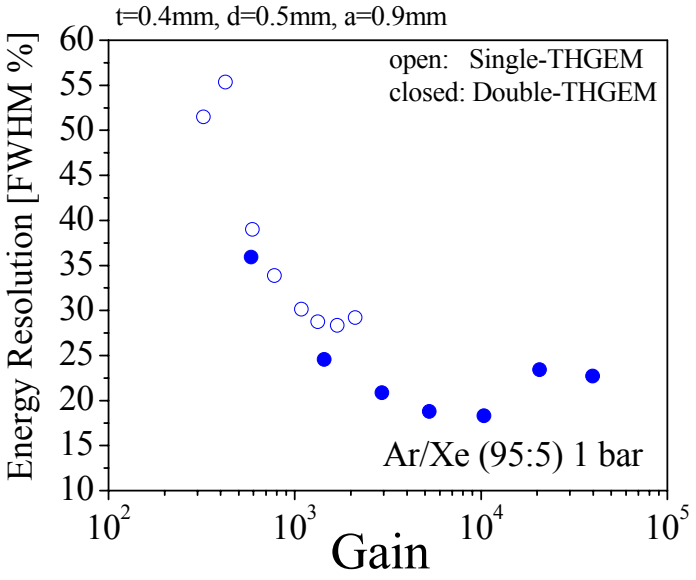

Figure 63: Energy resolution versus gain in single- and double-THGEM detector operated in 1 bar Ar/Xe (95:5)

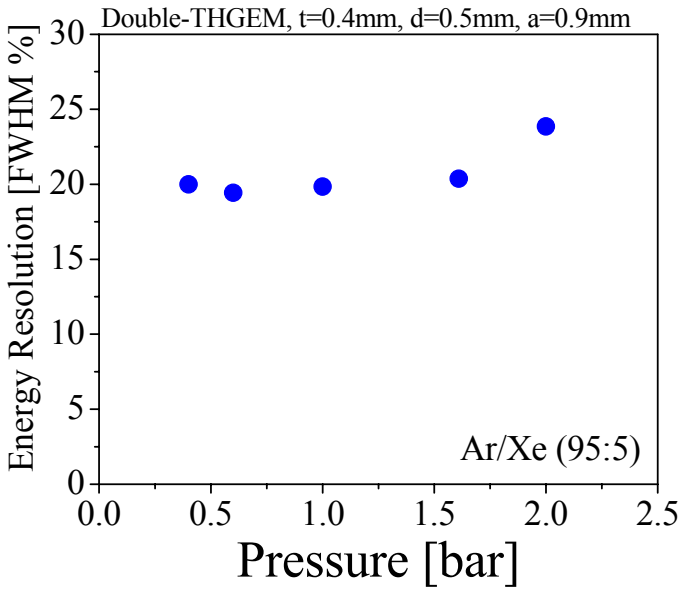

Figure 64: Energy resolution versus pressure in a double-THGEM detector in Ar/Xe (95:5). Drift field is 100 V/cm. Detector gain ~10^4.

5.4 Simulations

Aside from electron transfer efficiency, the energy resolution depends on the multiplication mechanism, and specifically on its uniformity. Due to the dipole nature of the hole field, there is always field penetration [8] from the hole into the gaps above and below the THGEM, which depends on the hole geometry and the field strength across the hole and in the gaps. This field penetration can affect the energy resolution. To understand the dependence of the energy resolution on the geometry and the electric field we carried out a simulation study of the electric field magnitude inside and outside the hole, using Maxwell 3D [18]; the study was done for different hole diameters, keeping a fixed gain (10^4); the maximum field value inside the hole was about the same for all geometries, but its shape differed. A multiplication threshold was set to electric fields above 5 kV/cm, corresponding to an approximate onset of charge multiplication in the investigated gases [64, 65]. As an estimate of the field penetration outside the hole, the integrated area under the electric field curve was used, as seen in Figure 65 (a). The field penetration ratio, i.e. the ratio between the area under the curve where the field is above the threshold and outside the hole (striped areas in Figure 65 a), to the area under the curve where the field is above the threshold (sum of striped and dark areas in Figure 65 a) was calculated.

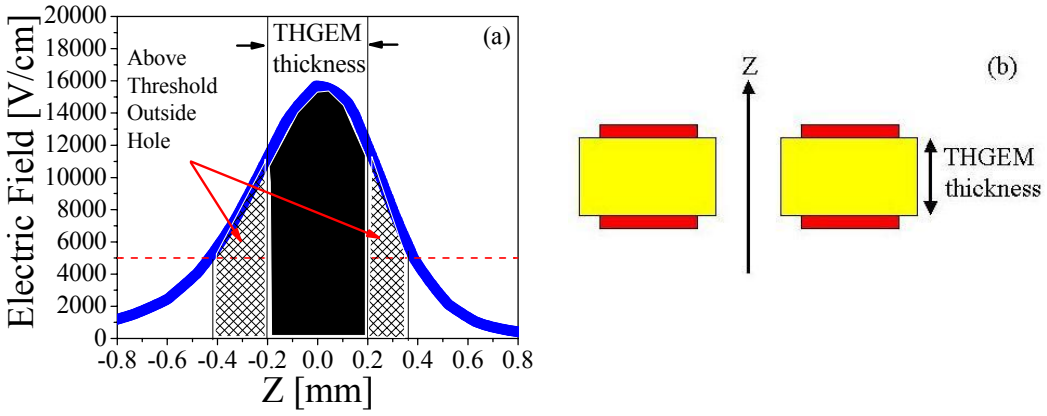

Figure 65: Maxwell [18] simulation results (a) of the electric field inside the THGEM hole along its Z axis (shown in b), at 1 bar. The chosen multiplication threshold is indicated by a dashed line, and the multiplication region is indicated by the dark and striped areas, inside and outside the hole, respectively. The field penetration ratio is the striped area divided by the sum of the striped and the dark areas.

Figure 66 shows the field penetration ratio versus the hole diameter for three different THGEM thicknesses. The 0.6mm thick electrode was not used in any of the experiments; its simulation results are shown for comparison.

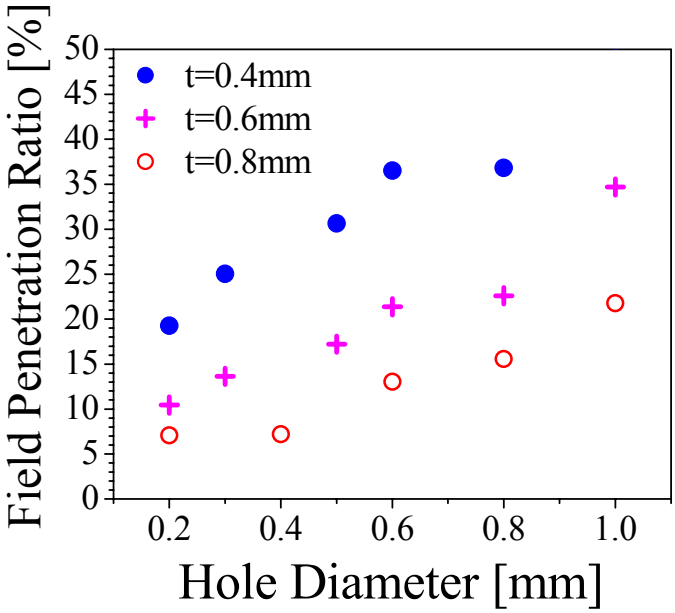

Figure 66: Ratio of field outside the hole and above threshold, to the field above threshold, versus hole diameter for different THGEM thicknesses.

5.5 Discussion of the operation in Ar, Xe and Ar/Xe

Measurements in this work were done at room temperature, with single- and double-THGEM detectors, with electrodes having various geometric parameters presented in

Table 3. Gains above 10^4 were reached practically in all geometries, in all gases investigated at 1 bar: Ar, Xe and Ar/Xe (95:5). The dependence of the maximum-gain in 1 bar Ar on the hole diameter, measured with 5.9 keV x-rays, (Figure 67) indicates that the maximum gain was achieved with holes smaller than 0.6mm in diameter. The gain limit for the larger-diameter holes could be explained by larger electric-field penetration from the hole into the surrounding gaps, shown in Figure 68; the latter requires operation at higher voltages for reaching similar gains; it also causes avalanche extension outside the holes, accompanied by photon emission – inducing secondary effects. Measurements in Xe were performed over a pressure range of 0.5-2.9 bar; an increasing drop in the maximum achievable gain was observed at pressures >2 bar, as shown in Figure 55. In Ar/Xe (95:5), gains above 10^4 were measured practically over the entire pressure range 0.1 – 2 bar (Figure 57). The higher gain at 2 bar compared to that reached in Xe could be explained by the significantly lower operation voltages in this Penning mixture.

It should be noted that in some cases (particularly in Ar as seen in curve 1 in Figure 53) the detector's gain limit was lower after evacuating the detector vessel to high vacuum conditions, prior to gas introduction. This is attributed to the absence of impurities, which often act as avalanche-photon "quenchers". The effect of the quencher is more beneficial in Ar, which emits more energetic avalanche photons compared to Xe (at wavelengths of ~120 nm for Ar compared to ~170 nm for Xe); these photons induce secondary effects (e.g. photoelectron emission from electrodes and walls) which limit the operation stability at higher gain. Lower gain limits at high gas purity could also result, to some extent, from charging up of the electrode's FR4 substrate which after extended pumping (e.g. of water molecules) may have an increased surface resistivity. These effects are the subject of current studies. After evacuation followed by gas filling and circulation through getters, 20-fold higher gains were reached with the Penning mixture [61, 62] of Ar/Xe (95:5) compared to those of pure Ar.

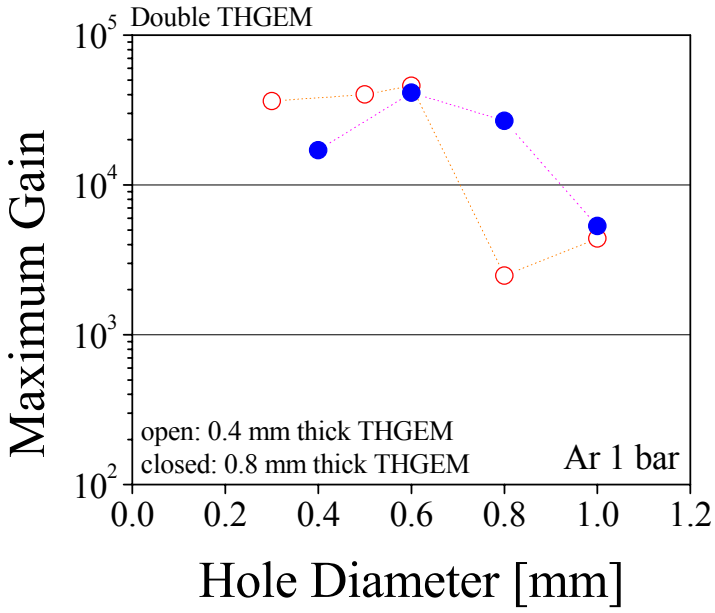

Figure 67: Maximum gain versus hole diameter measured with double-THGEM in 1 bar Ar for 0.4 and 0.8 thick THGEM plates

At cryogenic temperatures, the maximum achievable gain in all gases is expected to drop due to the increase in gas density, as recently demonstrated with cascaded GEMs [48, 49] and in Resistive Electrode Thick GEMs (RETGEM) [59].

Best energy resolutions reached in Ar with 5.9 keV x-rays using double-THGEM were of the order of 30% FWHM. These results are similar to those recently measured with RETGEM in Ar at similar working conditions [68]. The resolution in Xe for 5.9 keV x-rays using single-THGEM reached values of 21%-22% FWHM over the pressure range of 0.5-1 bar, respectively, and 27% using double-THGEM. In Ar/Xe (95:5) Penning mixture a better energy resolution was measured, of ~20% FWHM in a double-THGEM over the pressure range of 0.4 – 2 bar with a slight increase to ~24% at 2 bar (Figure 64).

The difference between the energy resolutions measured in the different gases originates from the differences in the statistical fluctuations in the numbers of primary and avalanche electrons; these are function of the W-values (the average energy per an electron-ion pair) [67], Fano factors [65, 67] and the parameters characterizing avalanche statistics [12, 69]. The high gains reached in Ar/Xe (95:5) at low multiplication fields and the superior energy resolutions result from the lower W-

value of 23.2 eV [67], and wave-length shifting of the high energy avalanche photons of Ar to Xe wavelengths.

The best energy resolutions in 1 bar Ar were achieved with holes smaller than 0.6 mm in diameter. THGEM plates of thickness 0.4 mm with 1 mm diameter holes (results not shown) yielded energy resolutions of 46% and lower gains. The electric field penetration from larger-diameter holes into the surrounding gaps causes gain fluctuations due to partial amplification outside the hole, affecting the energy resolution.

It was shown earlier, in other multiplication geometries [70], that the avalanche fluctuations are reduced at smaller avalanche-formation volumes. This supports the better energy resolution observed with smaller-diameter holes.

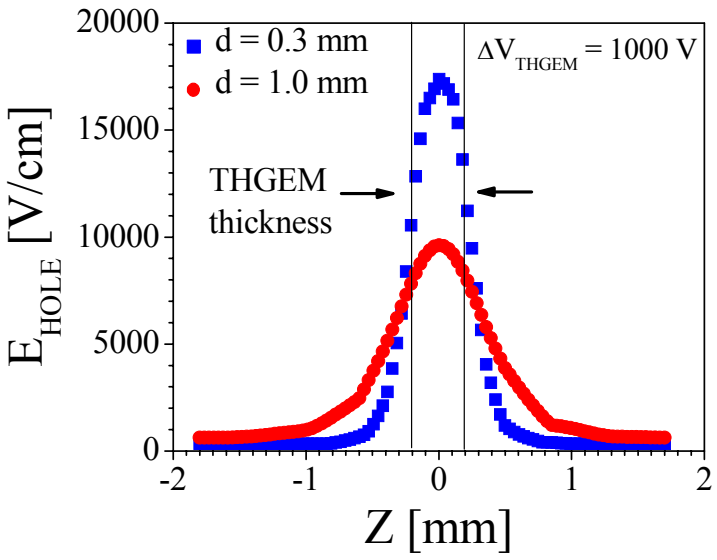

Figure 68: Maxwell [18] simulation of the electric field inside the THGEM hole along the Z axis for two different hole diameters. THGEM thickness: 0.4mm; potential across the hole: 1000V

Figure 66 clearly indicates that for a constant gain, for each THGEM plate thickness, the field penetration ratio increases with hole diameter. For a constant hole diameter, the field penetration decreases with the THGEM plate thickness. This may explain the difference in the slopes of the energy resolution versus drift-field plots shown in Figure 60 (a) and (b). Since the field penetration is less significant with the 0.8 mm thick electrode (for equal hole diameter), the energy resolution is less dependent on the drift field, compared to that of the 0.4 mm thick electrode.

The energy resolution dependence on the drift field has a clear minimum, both in Ar and in Xe (Figure 60 and Figure 61). A drift-field correlated behavior of the charge collection into the holes, affecting energy resolution, was also observed in GEM detectors [71]. At low drift fields primary electrons are lost due to diffusion and recombination. Transverse diffusion coefficient in Ar has a minimum value at electric fields around 200 V/cm which matches the experimental energy resolution results [72]. At higher field values electrons can be lost due to their collection on the first THGEM top (cathode) electrode instead of entering into the holes. Figure 60(a) and Figure 61 show constant values of the energy resolution over a broad range of the drift field. The resolution changes more drastically in Figure 60(b) with the thinner THGEM. This may also be attributed to the stronger field penetration in the case of thinner THGEM plates, as shown in Figure 66.

Although higher gains and improved energy resolution were demonstrated in this work with the Ar/Xe (95:5) Penning mixture, it is probably not usable in the gas phase of a two-phase detector; it would cause unnecessary elevated pressure of Ar in a LXe-based detector. A possible LAr detector with dissolved Xe from a Ar/Xe mixture, indeed would not require Xe concentration of 5% as used in this work. Even with much lower Xe additives, the Penning effect exists and minute fractions of dissolved Xe in LAr will shift the photon spectrum into that of Xe.

In the case of the LXe detector a possible solution would also be other Penning mixtures based on Xe as parent gas. The results of such studies in Xe/CH_4 were reported in [48].

Figure 69 shows the dependence of the gain and energy resolution in the hole diameter to thickness ratio, for 1 bar Ar. For 0.4mm thick electrodes, the gain peaks at a ratio of 1.5 and drops sharply for higher ratios. Similar effect is observable at a ratio of 0.75 for 0.8mm thick electrodes. For both thicknesses, the energy resolution worsens as this ratio increases, with a significant jump at ratio of 2 for the 0.4mm thick electrodes.

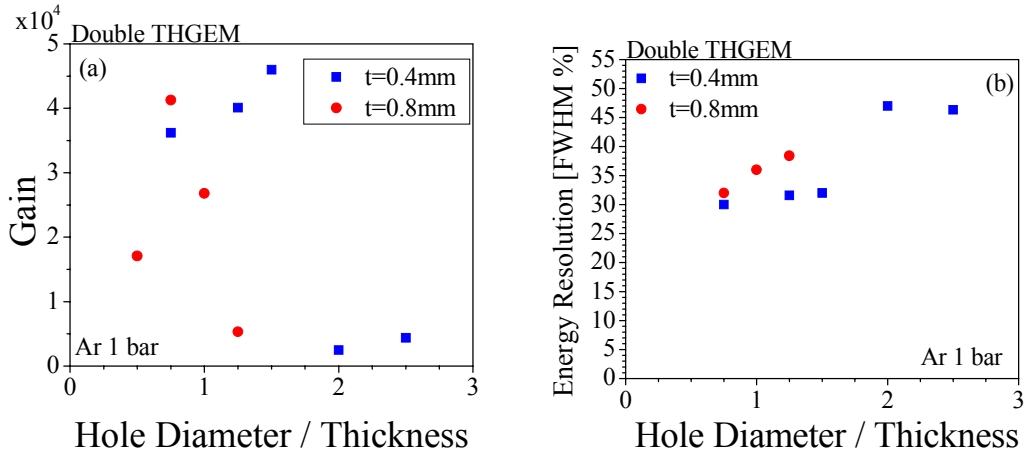

Figure 69: Gain (a) and energy resolution (b) versus hole diameter to thickness ratio in 1 bar Ar.

6. Summary

The THGEM is a robust easy-to-manufacture gaseous radiation detector, as demonstrated in our earlier works. Several, newly investigated aspects of the THGEM detector operation were presented in this work, namely time resolution, radiation imaging and operation in noble gases.

Time resolution was measured for the first time, with a double-THGEM detector. With single UV photons, a resolution of 8ns-10ns RMS was measured; with light pulses of over 1000 photons the time resolution was about 0.5ns RMS. With relativistic electrons from a ^{106}Ru source, a resolution of 12.7ns RMS was measured, while that with cosmic rays was 9.8ns RMS. The analysis of the fast MIPs signals proved to be difficult; the intrinsic time resolution should improve with better electronics and in measurements with accelerator beams.

The THGEM has shown good imaging performance. The detector had good high signal-to-noise properties, uniform gain across the sensitive area, and PSF width of 0.7mm FWHM (for hole pitch of 1mm). Preliminary investigations with fast neutrons, using detectors with imperfect THGEM electrodes, yielded worse spatial resolution, of 1.12mm FWHM. THGEM-based detectors may therefore become an attractive alternative solution for numerous applications, where large-area radiation imaging detectors with modest (sub-mm) position resolution are required.

The operation of THGEM-based detectors in noble gases, at room temperature was studied in atmospheric pressure of Ar, in the pressure range of 0.5-2.9 bar with Xe and in 0.1-2 bar of Ar/Xe (95:5). The geometrical parameters of the THGEM electrodes were optimized for noble-gas operation. Gains of 10^4 were obtained with 5.9 keV x-rays in all gases in almost all tested configurations at atmospheric pressure. Energy resolutions of 18.8%, 27% and 30% were measured in Ar/Xe (95:5), Xe and Ar respectively.

The results pave the way towards more extensive studies planned at cryogenic temperatures for evaluating the operation properties of such electrodes in two-phase (noble liquid/gas) detectors. THGEM-based two-phase detectors could be good candidates for ionization and scintillation signals recording in large-volume Dark-Matter and neutrino experiments, and in gamma-cameras for PET. In this operation mode, THGEMs are expected to offer more stable operation in cryogenic conditions

due to lower condensation effects in the ten-fold larger holes compared to GEMs. THGEM electrodes of low-radioactivity materials, e.g. Cirlex, have been investigated for these rare-event experiments; they are expected to yield a more economic solution for large-volume detectors and significantly lower radioactive background compared to photomultiplier tubes. A R&D project of a liquid-xenon Gamma Camera for medical imaging, incorporating THGEM photon detectors, is also in course at our laboratory.

References

[1] F. Sauli, *Micro-pattern gas detectors*, Nucl. Inst. Meth. A 477 (2002) 1-7.

[2] A. Oed, *Position-sensitive detector with microstrip anode for electron multiplication with gases*, Nucl. Inst. and Meth. A 263 (1988) 351-359.

[3] F. Sauli, *GEM: A new concept for electron amplification in gas detectors*, Nucl. Inst. and Meth. A 386 (1997) 531-534.

[4] Y. Giomataris et al., *MICROMEGAS: a high-granularity position-sensitive gaseous detector for high particle-flux environments*, Nucl. Inst. and Meth. A 376 (1996) 29-35.

[5] R. Chechik et al., *Thick GEM-like hole multipliers: properties and possible applications*, Nucl. Inst. and Meth. A 535 (2004) 303-308.

[6] R. Chechik et al., *Thick GEM-like multipliers - a simple solution for large area UV-RICH detectors*, Nucl. Inst. and Meth. A 553 (2005) 35-40.

[7] R. Chechik et al, *Thick GEM-like (THGEM) detectors and their possible applications*, Proc. of the SNIC Symposium on novel detectors, Stanford, Ca-USA, April 2006; article #25. http://www.slac.stanford.edu/econf/C0604032/papers/0025.PDF

[8] C. Shalem et. al., *Advances in Thick GEM-like gaseous electron multipliers-Part I: atmospheric pressure operation*, Nucl. Inst. and Meth. A 558 (2006) 475-489.

[9] C. Shalem et. al., *Advances in Thick GEM-like gaseous electron multipliers-Part II: Low-pressure operation*, Nucl. Inst. and Meth. A 558 (2006) 468-474.

[10] C. Shalem, *R&D of a novel gas electron multiplier – the THGEM*, MSc degree thesis accepted by the Weizmann Institute, Israel, in 2005, 2005 JINST TH 001.

[11] M. Cortesi et al., Investigation of a THGEM-based detector, JINST 2 (2007) P09002, and references therein.

[12] G.F. Knoll, *Radiation Detection And Measurement*, John Wiley & Sons, 1979.

[13] L. Lopes et al., *Accurate timing of gamma rays with high-rate Resistive Plate Chambers*, Nucl. Inst. and Meth. A 573 (2007) 4-7.

[14] G. Bencivenni et al., *A fast multi-GEM-based detector for high-rate charged-particle triggering*, IEEE TNS 49 (2002) 3242-3246.

[15] M. Alfonsi et al., *High-rate particle triggering with triple-GEM detector*, Nucl. Inst. and Meth. A 518 (2004) 106-112.

[16] D. Mörmann, *Study of novel gaseous photomultipliers for UV and visible light*, PhD degree thesis accepted by the Weizmann Institute, Israel, in 2005, 2005 JINST TH 004.

[17] R.A. Wijsman, *Breakdown Probability of a Low Pressure Discharge*, Physical Review 75 (1949) 833-838.

[18] MAXWELL 3D, ANSFOT Co. Pittsburg, PA, USA.

[19] GARFIELD, simulation program for gaseous detectors written by R. Veenhof, CERN, version 9

[20] http://consult.cern.ch/writeup/garfield/examples/gas/ArCH4.html

[21] F. Sauli, *Principles Of Operation Of Multiwire Proportional And Drift Chambers*, CERN, yellow report 77-09, 1977.

[22] http://physics.nist.gov/PhysRefData/Star/Text/ESTAR.html

[23] *Isotopes*, V/O Sojuzchimexport, Moscu, g-200, URSS.

[24] F. Sauli, *Micro-pattern gas detectors*, Nucl. Inst. and Meth. A 477 (2002) 1-7.

[25] A. Oed, *Micro pattern structures for gas detectors*, Nucl. Inst. and Meth. A 471 (2001) 109-114.

[26] V. Dangendorf et al., *Detector for time-of-flight fast-neutron radiography: 1 neutron counting gas detector*, Nucl. Inst. and Meth. A542 (2005) 197-205

[27] ACAM-Messelectronic GmbH, http://ww.acam.de.

[28] MQT300A, CHARGE-TO-TIME CONVERTER, LeCroy 1999, http://www.lecroy.com/

[29] CAMDA, A small CAMAC Data Acquisition System, Herbert Stelzer, GSI Darmstadt, Germany.

[31] D.N. Sitter et al., *Method for the measurement of the modulation transfer function of sampled imaging systems from bar-target patterns*, Applied Optics, volume 34 (1995) 746-751

[31] V. J Lehr et al., *Image restoration in X-ray microscopy: PSF determination and biological applications*, IEEE Trans on Image Processing, 7(2) (1998) 258-263.

[32] V. Dangendorf et al., *Detectors for energy-resolved fast-neutron imaging,* Nucl. Inst. and Meth. A 535 (2004) 93-97, and references therein.

[33] V. Dangendorf et al., *Detectors for time-of-flight fast-neutron radiography 1. Neutron-counting gas detector,* Nucl. Inst. and Meth. A 542 (2005) 197-205.

[34] D. Vartsky et al., *Time-resolved fast neutron imaging: simulations of detector performance*, Nucl. Inst. and Meth. A 542 (2005) 206-212.

[35] J. W. Coltman, *The Specification of Imaging Properties by Response to a Sine Wave Target*, Journal of the Optical Society of America 44 (1954) 468-471.

[36] L.M. Logory et. al., *Characterization of an x-ray framing camera utilizing a charge coupled device or film as recording media*, Review Of Scientific Instruments, 69 (1998) 4054.

[37] N.B. Nill, *Conversion Between Sine Wave and Square Wave Spatial Frequency Response of an Imaging System*, MITRE technical papers, MTR01B0000021 (2001).

[38] R. Alon et al, *Operation of a Thick Gas Electron Multiplier (THGEM) in Ar, Xe and Ar-Xe*, JINST 3 (2008) P01005.

[39] Super-Kamiokande Collaboration, *Evidence of Oscillation of Atmospheric Neutrinos*, Phys. Rev. Lett. 81 (1998) 1562-1567.

[40] SNO Collaboration, *Direct Evidence for Neutrino Flavor Transformation from Neutral-Current Interactions in the Sudbury Neutrino Observatory*, Phys. Rev. Lett. 89 (2002) 011301.

[41] KamLAND Collaboration, *First Results from KamLAND: Evidence for Reactor Antineutrino Disappearance*, Phys. Rev. Lett. 90 (2003) 021802.

[42] CDMS Collaboration, *New results from the Cryogenic Dark Matter Search experiment*, Phys. Rev. D 68 (2003) 82002.

[43] Edelweiss Collaboration, *Improved exclusion limits from the EDELWEISS WIMP search*, Phys. Lett. B 545 (2002) 43.

[44] J. Angle et al., *First Results from the XENON10 Dark Matter Experiment at the Gran Sasso National Laboratory*, Phys. Rev. Lett. 100 (2008) 021303.

[45] EXO Collaboration, M. Danilov et al., *Detection of very small neutrino masses in double-beta decay using laser tagging,* Phys. Lett. B 480 (2000) 12-18.

[46] B.A. Dolgoshein et al., *New method of registration of ionizing-particle tracks in condensed matter*, JETP Lett. 11 (1970) 513.

[47] D. Cline et al., *A WIMP detector with two-phase xenon*, Astroparticle Physics 12 (2000) 373-377.

[48] A. Bondar et al., *Two-phase argon and xenon avalanche detectors based on Gas Electron Multipliers*, Nucl. Inst. and Meth. A 556 (2006) 273-280 and references therein.

[49] V. Solovov et al., *Operation of gas electron multipliers in pure xenon at low temperatures*, Nucl. Inst. and Meth. A 580 (2007) 331-334.

[50] G.J. Alner et al., *First limits on WIMP nuclear recoil signals in ZEPLIN-II: A two-phase xenon detector for dark matter detection*, Nucl. Inst. and Meth. A 28 (2007) 287-302.

[51] A. Breskin, *CsI UV photocathodes: history and mystery*, Nucl. Inst. and Meth. A 371 (1996) 116-136 and references therein.

[52] E. Aprile et al., *Electron extraction from a CsI photocathode into condensed Xe, Kr and Ar*, Nucl. Inst. and Meth. A 343 (1994) 129-134.

[53] V. Dangendorf et al., *A gas-filled UV-photon detector with CsI photocathode for the detection of Xe light*, Nucl. Inst. and Meth. A 289 (1990) 322-324.

[54] T. Meinschad et al., *Detection of primary and field-enhanced scintillation in xenon with a CsI-coated GEM detector*, Nucl. Inst. and Meth. A 547 (2005) 342-345.

[55] A Bondar et al., *Further studies of two-phase krypton detectors based on Gas Electron Multipliers*, Nucl. Inst. and Meth. A 548 (2005) 439-445.

[56] L. Periale et al., *Detection of primary scintillation light from dense Ar, Kr and Xe with novel photosensitive gaseous detectors*, Nucl. Inst. and Meth. A 478 (2002) 377-383.

[57] P. Jeanneret, *Time Projection Chambers and detection of neutrinos*, Ph.D. Thesis Neuchâtel Univ. 2001.

[58] R. Lüscher et al., *Dark matter search at Boulby mine*, EPJ C 33 (2004) 968-970.

[59] A. Di Mauro et al., *Development of innovative micro-pattern gaseous detectors with resistive electrodes and first results of their applications*, Nucl. Inst. and Meth. A 581 (2007) 225-231.

[60] M.Gai et al., *Toward application of a thick gas electron multiplier (THGEM) readout for a dark matter detector,* Proc. 23rd Winter Workshop on Nuclear Dynamics, Big Sky, Montana, USA, Feb. 11-18, 2007. http://arxiv.org/abs/0706.1106.

[61] F.L.R. Vinagre et al., *Penning Effects in Ar-Xe Mixtures at Atmospheric Pressures: Absolute W-Value Measurements for 5.9 keV X-Rays*, Nuclear Science Symposium, 1999. Conference Record. 1999 IEEE 2 (1999) 651-653.

[62] Buzulutskov et al., *The GEM photomultiplier operated with noble gas mixtures*, Nucl. Inst. and Meth. A 443 (2000) 164-180.

[63] F.I.G.M. Borges et al., *Operation of gas proportional scintillation counters in a low charge multiplication regime*, Nucl. Inst. and Meth. A 422 (1999) 321-325.

[64] C.M.B. Monteiro et al., *An Argon Gas Proportional Scintillation Counter With UV Avalanche Photodiodes Scintillation Readout*, IEEE Tran. on Nucl. Sci. 48 (2001) 1081-1086.

[65] V. Solovov et al., *Operation of gas electron multipliers in pure xenon at low temperatures*, Nucl. Inst. and Meth. A 580 (2007) 331-334.

[66] E.P. de Lima et al., *Fano factors of rare gases and their mixtures*, Nucl. Inst. and Meth. 192 (1982) 575-581 and references therein.

[67] R. Oliveira et al., *First tests of thick GEMs with electrodes made of a resistive kapton*, Nucl. Inst. and Meth. A 576 (2007) 362-366.

[68] P.J.B.M. Rachinhas et al., *Energy resolution of xenon proportional counters: Monte Carlo simulation and experimental results*, IEEE Tran. on Nucl. Sci. 43 (1996) 2399-2405.

[69] G.D. Alkhazov, *Statistics of electron avalanches and ultimate resolution of proportional counters*, Nucl. Inst. and Meth. 89 (1970) 155-165.

[70] S. Bachmann et al., *Charge amplification and transfer processes in the gas electron multiplier*, Nucl. Inst. and Meth. A 438 (1999) 376-408.

[71] http://consult.cern.ch/writeup/garfield/examples/gas/ArCH4.html - diff